The Astrophysical Journal, 871:128 (19pp), 2019 January 20 https://doi.org/10.3847/1538-4357/aaf386

Dust Attenuation, Star Formation, and Metallicity in $z \sim 2$–3 Galaxies from KBSS-MOSFIRE

Rachel L. Theios[1], Charles C. Steidel[1], Allison L. Strom[2], Gwen C. Rudie[2], Ryan F. Trainor[3], and Naveen A. Reddy[4]
[1] Cahill Center for Astronomy and Astrophysics, California Institute of Technology, 1200 East California Boulevard, MC 249-17 Pasadena, CA 91125, USA; rtheios@astro.caltech.edu
[2] Carnegie Observatories, 813 Santa Barbara Street, Pasadena, CA 91101, USA
[3] Physics and Astronomy Department, Franklin & Marshall College, 415 Harrisburg Pike, Lancaster, PA 17603, USA
[4] Department of Physics and Astronomy, University of California, Riverside, 900 University Avenue, Riverside, CA 92521, USA
Received 2018 April 30; revised 2018 November 8; accepted 2018 November 21; published 2019 January 25

Abstract

We present a detailed analysis of 317 $2.0 \leqslant z \leqslant 2.7$ star-forming galaxies from the Keck Baryonic Structure Survey. Using complementary spectroscopic observations with Keck/LRIS and Keck/MOSFIRE, as well as spectral energy distribution (SED) fits to broadband photometry, we examine the joint rest-UV and rest-optical properties of the same galaxies, including stellar and nebular dust attenuation, metallicity, and star formation rate (SFR). The inferred parameters of the stellar population (reddening, age, SFR, and stellar mass) are strongly dependent on the details of the assumed stellar population model and the shape of the attenuation curve. Nebular reddening is generally larger than continuum reddening, but with large scatter. Compared to local galaxies, high-redshift galaxies have lower gas-phase metallicities (and/or higher nebular excitation) at fixed nebular reddening, and higher nebular reddening at fixed stellar mass, consistent with gas fractions that increase with redshift. We find that continuum reddening is correlated with $12 + \log(\mathrm{O/H})_{\mathrm{O3N2}}$ at 3.0σ significance, whereas nebular reddening is correlated with only 1.1σ significance. This may reflect the dependence of both continuum reddening and O3N2 on the shape of the ionizing radiation field produced by the massive stars. Finally, we show that Hα-based and SED-based estimates of SFR exhibit significant scatter relative to one another, and on average agree only for particular combinations of spectral synthesis models and attenuation curves. We find that the SMC extinction curve predicts consistent SFRs if we assume the subsolar ($0.14\,Z_{\odot}$) binary star models that are favored for high-redshift galaxies.

Key words: dust, extinction – galaxies: evolution – galaxies: high-redshift – galaxies: star formation – HII regions – ISM: abundances

1. Introduction

It is well-established that much of the stellar mass in the universe formed at $z > 1$ and that star-forming systems dominate the galaxy population at this epoch (Madau & Dickinson 2014). Constraining details of the cosmic star formation rate evolution has long been a focus of extragalactic astrophysics, but it is a complex issue, as estimates of star formation rate (SFR) are subject to uncertainties in a wide variety of parameters, including dust attenuation corrections, the timescale of the current episode of star formation, the ionizing photon production rate (used to estimate SFRs from Hα luminosities), and the assumed stellar initial mass function (IMF).

In order to recover the intrinsic SFR of a galaxy, one must first determine the effect of dust obscuration on the observations used to measure it. However, this determination is not always straightforward, as both the rest-UV stellar continuum and nebular emission lines can be used to estimate the SFR at high redshift (in cases where far-IR measurements are not available), and these two SFR indicators necessitate different measures of the dust attenuation correction. Generally, such corrections involve measuring the dust reddening $E(B-V)$ relative to an SED template and translating it to an attenuation in magnitudes A_{λ}, assuming some attenuation curve, usually parameterized by the quantity $k(\lambda)$, which is defined such that $k(\lambda) = A_{\lambda}/E(B-V)$.

Attenuation affecting the far-UV stellar continuum has been estimated using a variety of methods, including the so-called IRX-β relation, where the UV continuum slope β, sensitive to the reddening, is correlated with the ratio $L_{\mathrm{IR}}/L_{\mathrm{UV}}$ (IRX), which traces the attenuation (Calzetti et al. 1994; Meurer et al. 1999; Adelberger & Steidel 2000; Reddy et al. 2006, 2010, 2012a, 2012b; Buat et al. 2011). Similarly, continuum attenuation can be measured by SFR comparisons (Erb et al. 2006; Daddi et al. 2007; Reddy et al. 2010, 2012b) and SED fitting to broad- and medium-band photometry using stellar population synthesis (SPS) models (Kriek & Conroy 2013; Reddy et al. 2015). At high redshift, the UV slope has been shown to be a reasonable tracer of dust attenuation on average (e.g., Reddy et al. 2006, 2010, 2012a; Daddi et al. 2007), although it is also sensitive to the stellar population age, metallicity, star formation history (SFH), IMF, and binarity (Reddy et al. 2015, and references therein). Continuum reddening $E(B-V)_{\mathrm{cont}}$ traces the integrated dust reddening toward those stellar populations primarily emitting in the FUV–NUV continuum.

The standard method for measuring dust attenuation toward star-forming regions in local galaxies involves comparing the Balmer decrement (BD)—the observed ratio $I(\mathrm{H}\alpha)/I(\mathrm{H}\beta)$—to the intrinsic value expected with no nebular reddening, $I(\mathrm{H}\alpha)/I(\mathrm{H}\beta) = 2.86$ for $T_e = 10{,}000$ K and Case B recombination (Osterbrock 1989). With an assumption of a line-of-sight extinction relation, such as the Milky Way curve of Cardelli et al. (1989), the BD is used to derive a value of nebular reddening $E(B-V)_{\mathrm{neb}}$, i.e., the reddening along the line of sight toward ionized nebulae, which is then translated into a dust correction. At $z > 1$, however, Hα and Hβ are redshifted to near-IR wavelengths, where observations have historically

been more difficult to obtain than in the optical. In recent years, with the advances made by slitless and multi-object near-IR spectrographs on the *Hubble Space Telescope* (*HST*) and 8–10 m class ground-based telescopes, it has become feasible to directly measure the BD for large samples of galaxies at intermediate and high redshift (e.g., Price et al. 2014; Reddy et al. 2015; Nelson et al. 2016; Strom et al. 2017).

Although the general consensus is that $E(B-V)_{\rm neb}$ should be used to derive a dust correction for emission lines and $E(B-V)_{\rm cont}$ should be used to derive a dust correction for the continuum, the relationship between these two quantities remains uncertain at high redshift, as both values depend on the details of the assumed massive stellar populations. The detailed relationship between nebular and continuum reddening also depends on complex effects, such as dust/star geometry and the starburst age distribution.

There is an extensive body of literature comparing $E(B-V)_{\rm neb}$ and $E(B-V)_{\rm cont}$ (e.g., Calzetti et al. 2000; Kashino et al. 2013; Price et al. 2014; Reddy et al. 2015; Shivaei et al. 2016), with far-from-uniform results. Calzetti et al. (2000) found that, in nearby starburst galaxies, reddening is higher toward star-forming regions, and on average $E(B-V)_{\rm neb} = 2.27E(B-V)_{\rm cont}$, where $E(B-V)_{\rm cont}$ is derived using the Calzetti et al. (2000) starburst attenuation relation, and $E(B-V)_{\rm neb}$ assumes a line-of-sight relation, such as the Galactic extinction curve of Cardelli et al. (1989).[5] At intermediate and high redshift ($z\sim1.5$–3), some studies have found that reddening is higher toward star-forming regions relative to the stellar populations producing the FUV–NUV continuum, where both the nebulae and the stellar continuum are assumed to be reddened using attenuation curves established at low redshift (e.g., Kashino et al. 2013; Price et al. 2014; Reddy et al. 2015). Other studies have found that the assumption $E(B-V)_{\rm neb}\approx E(B-V)_{\rm cont}$ is sufficient to produce consistent SFRs between observations of Hα and X-ray, mid-IR, and far-IR observations of similarly selected galaxies at $z\sim2$ (Reddy & Steidel 2004; Erb et al. 2006; Reddy et al. 2006, 2010, 2012a; Daddi et al. 2007).

This issue is further complicated by the fact that the many different factors relating $E(B-V)_{\rm neb}$ to $E(B-V)_{\rm cont}$ in the literature assume different attenuation curves, and thus cannot be compared directly. Many studies have used $E(B-V)_{\rm cont}$ as a proxy for $E(B-V)_{\rm neb}$ when direct measurements of the BD are not available, which requires an assumption of a translation between nebular and continuum reddening, as in Calzetti et al. (2000). However, Steidel et al. (2014) noted that the equation relating $E(B-V)_{\rm cont}$ to $E(B-V)_{\rm neb}$ given by Calzetti et al. (2000) is often misinterpreted to mean that the *attenuation* in magnitudes affecting an Hα photon is a factor of 2.27 higher than that affecting a continuum photon at the same wavelength. In fact, because the attenuation in magnitudes $A_\lambda = k(\lambda)E(B-V)$, where $k(\lambda)$ is the value of the attenuation or extinction relation at wavelength λ, the translation from a *reddening* relation to an *attenuation* relation requires an additional factor of $k(\lambda)$, which should be internally consistent with the attenuation or extinction curves used to derive each measure of $E(B-V)$.

Another issue that remains to be addressed is the appropriate continuum attenuation curve to apply to high-redshift galaxies. Several recent theoretical works (e.g., Narayanan et al. 2018; Salim et al. 2018) have have predicted the shape of the dust attenuation curve in high-redshift galaxies, as well as the relationship between attenuation and extinction curves, with varying results. On the observational side, some recent studies (e.g., Álvarez-Márquez et al. 2016; Reddy et al. 2018) have found that the application of the SMC curve to the UV continuum best reproduces the conditions in high-redshift galaxies, while other studies (e.g., Koprowski et al. 2018; McLure et al. 2018) have argued that the Calzetti et al. (2000) curve remains the most applicable attenuation curve.

Even after the appropriate dust correction has been determined, measurement of the intrinsic SFR of a galaxy depends on other parameters in a potentially complex manner. It is well-known that estimates of SFR for individual galaxies using different indicators can vary widely, particularly for the dustiest galaxies with $L_{\rm bol}\gtrsim10^{12}L_\odot$ for which UV color-based methods systematically underpredict the SFR (e.g., Reddy et al. 2012b). Similarly, estimates of SFR may differ due to the timescale over which indicators are sensitive: Hα luminosity is sensitive only to the most massive and short-lived stars that produce most of the ionizing photons, while the FUV continuum (1000–2000 Å) may have significant contributions from stars with lifetimes up to ∼100 Myr. In detail, converting either an observation of Hα luminosity or a UV continuum slope to an SFR depends on the timescale of the current episode of star formation and the SFH over the preceding ∼100 Myr.

Perhaps more importantly, estimates of the SFR depend on the nature of the population of massive stars that dominates the EUV and FUV light. Recent studies (e.g., Steidel et al. 2016) have indicated that developments in our understanding of massive stars, such as the significant role of binary evolution, may lead to revised estimates of galaxy SFRs at high redshift. For the BPASSv2.2 models (Stanway & Eldridge 2018) used in this paper, the Hα luminosity per unit solar mass of stars formed per year is larger by a factor of ∼2 (once differences in IMF have been accounted for) compared to the canonical conversion often used in the literature (Kennicutt 1998; Kennicutt & Evans 2012). The canonical values are based on modeling of solar-metallicity nebulae (and single-star SPS models) that are likely appropriate for most $z\sim0$ galaxies; however, the ISM conditions at $z\sim2$ are quite different, characterized by lower gas-phase metallicities than $z\sim0$ galaxies at fixed stellar mass and harder ionizing radiation fields (Strom et al. 2017). Thus, comparing SFRs estimated from Hα luminosity, dust-corrected using the BD, to those estimated from the UV stellar continuum, dust-corrected using the UV continuum slope, can yield important insights into the nature of star formation at high redshift.

In this paper, we analyze a sample of 317 galaxies with $2.0\leqslant z\leqslant2.7$ observed as part of the Keck Baryonic Structure Survey (KBSS; Rudie et al. 2012; Steidel et al. 2014; Strom et al. 2017), with high-quality near-IR spectra from Keck/MOSFIRE (McLean et al. 2012) together with deep optical spectra obtained with Keck/LRIS (Oke et al. 1995; Steidel et al. 2004), providing complementary rest-frame optical and rest-frame UV spectra of the same objects. KBSS is a large, targeted spectroscopic survey designed to jointly probe galaxies and the surrounding intergalactic medium (IGM) and circumgalactic medium (CGM) at the peak epoch of galaxy assembly, $z\sim2$–3. The redshift range $2.0\leqslant z\leqslant2.7$ is ideal for ground-based observations due to the fortuitous placement of nebular emission lines with respect to atmospheric

[5] Calzetti et al. (2000) used the Seaton (1979) extinction law.

transmission windows. Additionally, at $2.0 \leqslant z \leqslant 2.7$, the FUV portion of galaxy spectra falls above the atmospheric cutoff near 3100 Å. Thus, this redshift range uniquely provides access to both the stellar FUV continuum and nebular emission lines, making it possible to directly compare stellar and nebular measures of reddening and star formation. Finally, the availability of strong nebular emission lines in this redshift range allows us to estimate gas-phase oxygen abundance using strong-line methods, as a function of stellar mass (M_*), SFR, and dust reddening.

The aim of this paper is to use a large sample of galaxies with BD measurements to determine the relationship between nebular and continuum reddening. We measure continuum reddening by both SED fitting and SPS fitting to rest-UV spectra, and we use comparisons of SFRs measured by different means to place constraints on the most appropriate attenuation curve for the UV continuum. We examine the effects of different assumptions of stellar population characteristics on estimates of SFR. Finally, we examine the correlation of reddening with stellar mass and gas-phase oxygen abundance as determined from strong-line indices.

The outline of the paper is as follows. In Section 2, we introduce the subset of the KBSS-MOSFIRE sample discussed in this paper, and Section 3 describes our methodology for modeling stellar populations and measuring galaxy parameters. In Section 4, we present composite rest-UV spectra to which we have fit spectral synthesis models. We examine the relationship between stellar and nebular dust attenuation in Section 5.1. We compare dust attenuation with inferred gas-phase oxygen abundance and stellar mass in Section 5.2. Section 5.4 compares SFRs inferred from Hα with those inferred from SED fitting. Section 6 discusses the implications of these results, and Section 7 summarizes our conclusions. Appendix A describes details of our SED fitting methodology, and Appendix B describes our methodology for fitting spectral synthesis models to rest-UV spectra.

Throughout the paper, we adopt a ΛCDM cosmology with $H_0 = 70$ km s^{-1} Mpc^{-1}, $\Omega_\Lambda = 0.7$, and $\Omega_m = 0.3$. Conversion relative to solar metallicity assumes $Z_\odot = 0.0142$ (where Z is the fraction of metals by mass), as in Asplund et al. (2009). Specific spectral features are referred to using their vacuum wavelengths, and magnitudes are given in the AB system.

2. Observations and Data

2.1. Photometric Observations

Photometric data in the KBSS survey fields include broad-band photometry in the optical ($U_nG\mathcal{R}$), near-IR (J, H, K_s, and WFC3-IR F140W and F160W), and mid-IR (*Spitzer*-Infrared Array Camera 3.6 and 4.5 μm). The near-IR photometry was corrected for the emission line contribution from Hα and [O III] using measured fluxes from MOSFIRE. Most KBSS galaxies are selected by their rest-UV colors using a $U_nG\mathcal{R}$ color selection scheme designed to select Lyman Break Galaxy analogues at $z \gtrsim 2$. While this color selection technique may bias the sample against massive, dusty galaxies, the inclusion of $\mathcal{R}K$ objects (discussed by Strom et al. 2017) alleviates this bias somewhat. Details of the photometric data and sample selection are described elsewhere (e.g., Adelberger et al. 2004; Steidel et al. 2004; Reddy et al. 2012b; Steidel et al. 2014; Strom et al. 2017).

2.2. LRIS Observations

Optical (rest-UV) spectra of KBSS galaxies were obtained with Keck/LRIS. LRIS observations in the KBSS survey fields have been obtained over the course of the past decade, and include observations with a variety of wavelength coverage, signal-to-noise ratio, and spectral resolution; for details, see Shapley et al. (2005), Steidel et al. (2010, 2016) , and Reddy et al. (2012b). Here, we used observations with the blue channel of LRIS (LRIS-B), using both the 600 line/mm grism, which achieves a resolving power of $R \sim 1400$ and covers the wavelength range 3300–5600 Å, and the 400 line/mm grism, which achieves $R \sim 800$, covers 3100–6200 Å, and is optimized for the highest throughput at wavelengths $\leqslant$4000 Å.

Due to the variable signal-to-noise ratio of the LRIS spectra used in this paper, we stack the spectra in bins of selected galaxy properties (see Appendix B for details). For the stacking analysis, the spectra were interpolated onto a common rest wavelength scale of 0.35 Å/pixel and averaged without weighting; the rest wavelength range $1100 \leqslant \lambda_0 \leqslant 1700$ Å was used for fitting. To test that the relative flux calibration of the LRIS spectra was consistent with the photometry, we generated composite spectra in bins of $E(B-V)$ (as inferred from SED fits to broadband photometry of individual objects), and fit stellar spectral synthesis models to the composites to infer a continuum $E(B-V)$. The two measures of continuum reddening are comparable.

2.3. MOSFIRE Observations

Near-IR (rest-optical) spectra of KBSS galaxies were obtained with Keck/MOSFIRE. The near-IR portion of the KBSS survey (KBSS-MOSFIRE) was designed to provide high-quality rest-optical spectra for galaxies in the KBSS survey fields with multiwavelength ancillary data as well as spectroscopic observations (primarily with LRIS-B). For a full description of KBSS-MOSFIRE observing strategies, data reduction, sample selection, and emission-line fitting, see Steidel et al. (2014) and Strom et al. (2017). In this work, we focus on the subset of KBSS-MOSFIRE galaxies with nebular redshifts $2.0 \lesssim z \lesssim 2.7$ in order to place important strong emission lines in the NIR atmospheric passbands, and with sufficiently deep H-band and K-band spectra to allow significant detections of the emission lines of interest: Hα λ6564.61 and [N II]λ6585.27 in the K band, and Hβ λ4862.72 and [O III]λ5008.24 in the H band. The Balmer lines have been corrected for underlying Balmer absorption based on the best-fit SED models, as detailed by Strom et al. (2017).

Of particular importance for the purposes of this paper is the issue of cross-band calibration—correcting emission line fluxes for relative slit losses so that the ratios of lines observed in different spectral bands are accurate. This cross-calibration is necessary for analyses involving the BD, as Hβ falls in H band and Hα in K band for galaxies over the redshift range of interest for this study, $2.0 \leqslant z \leqslant 2.7$. The method used to estimate slit losses is described in detail by Strom et al. (2017). In brief, the cross-calibration combines separate observations of the same objects on independent slit masks with observations of a bright star placed on each mask in order to correct for slit losses for each object in each observed band.

Table 1
Sample Statistics

Galaxy Sample	N_{gal}	z_{neb} (Mean)	Hα/Hβ (Median)
KBSS-MOSFIRE	1103	2.23	⋯
$2.0 \leqslant z \leqslant 2.7$	735	2.30	⋯
Hα+Hβ[a]	373	2.29	3.97 ± 1.90
Hα/H$\beta > 3\sigma$[b]	317	2.29	3.87 ± 1.60
[O III]+[N II][c]	270	2.29	3.88 ± 1.60
LRIS+MOSFIRE[d]	270	2.30	3.95 ± 1.83

Notes. Error bars on median values are the inter-quartile range.
[a] The subset of KBSS-MOSFIRE galaxies with $2.0 \leqslant z \leqslant 2.7$ and measurements of the BD Hα/Hβ at any significance.
[b] The main sample discussed in this paper is the subset of KBSS-MOSFIRE galaxies with $2.0 \leqslant z \leqslant 2.7$ and S/N > 3 on the BD Hα/Hβ, including slit loss uncertainties in *H* and *K*.
[c] The [O III]+[N II] sample is the subset of those galaxies with observations of [O III]λ5008 and [N II]λ6585, 32 of which are undetected ($<2\sigma$) in [N II]λ6585.
[d] The LRIS+MOSFIRE sample is the subset of galaxies with complementary LRIS observations. This sample and the [O III]+[N II] sample have the same number of N_{gal}, but this is coincidental, as there is not perfect overlap between the two samples.

2.4. Sample Statistics

The full KBSS sample consists of 2844 galaxies with spectroscopically confirmed redshifts in the range $1.5 \lesssim z \lesssim 3.5$, 2345 of which have existing rest-frame UV spectra from Keck/LRIS-B. As of 2016 December 1, the near-IR portion of KBSS (KBSS-MOSFIRE) consists of 1103 galaxies with nebular redshifts obtained from Keck/MOSFIRE. AGN have been removed from the sample, as discussed by Steidel et al. (2014) and Strom et al. (2017).

Table 1 and Figure 1 give an overview of the galaxy samples discussed in this paper. We selected 317 KBSS-MOSFIRE galaxies in the redshift range $2.0 \leqslant z \leqslant 2.7$ with robust detections of both Hα and Hβ (S/N > 3 for the line ratio Hα/Hβ). The motivation for a significance cut on the BD is discussed by Strom et al. (2017): because attenuation corrections scale nonlinearly with the measured value of the BD, relatively small uncertainties in the BD can translate to a large uncertainty in quantities that are dust-corrected using the BD, such as the SFR. In practice, requiring S/N > 3 in the ratio BD $\equiv I(\mathrm{H}\alpha)/I(\mathrm{H}\beta)$, including the relative slit loss uncertainties in *H* and *K*, means that S/N > 3 in Hα and Hβ individually. While it is possible that this significance cut biases the sample against the most heavily reddened objects, the median BD of the 3σ sample and the subset of 373 galaxies with measurements of BD at any significance are consistent within the errors (Table 1).

3. Derived Galaxy Properties

3.1. SED Fitting

Stellar masses, SFRs (hereafter $\mathrm{SFR_{SED}}$), and continuum color excesses (hereafter $E(B-V)_{\mathrm{SED}}$) were estimated for KBSS-MOSFIRE galaxies based on SED fits to broadband photometry described in Section 2.1.

The SED fitting uses reddened "Binary Population and Spectral Synthesis" (BPASSv2.2) models (Stanway & Eldridge 2018), assuming a constant SFH and a minimum allowed age of 50 Myr. As discussed by Reddy et al. (2012a), this minimum age is approximately the central dynamical timescale and is imposed to prevent best-fit solutions with unrealistically young ages.[6] The BPASSv2.2 model used as the fiducial model for the SED fitting has a stellar metallicity of $Z_* = 0.002$ ($Z_*/Z_\odot \approx 0.14$) and binary evolution included. The model we used has a Kroupa-type IMF, with a slope of -2.35 for masses $>1\,M_\odot$ and an upper mass cutoff of $100\,M_\odot$.

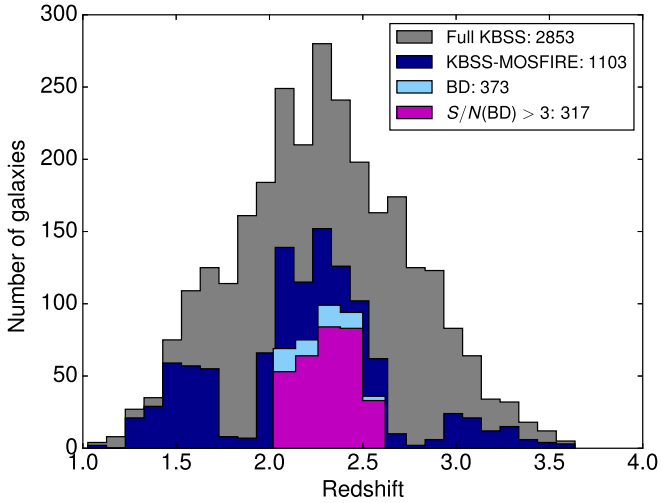

Figure 1. Redshift distributions of the galaxy samples discussed in this paper (see Table 1).

The main feature of the BPASSv2.2 models is the inclusion of massive interacting binary stars, increasing the overall ionizing flux and producing a harder ionizing spectrum for models with continuous SFHs. This is an advantage over previous models, not only because most massive stars are known to be in binaries (Crowther 2007; Sana et al. 2012), but also because previous studies (e.g., Reddy et al. 2016b; Steidel et al. 2016; Strom et al. 2017) have found that these models are able to simultaneously match the rest-UV stellar continuum and nebular emission lines better than single-star models. Additionally, Steidel et al. (2016) noted an important difference between the continuous star formation BPASS models including binary evolution and single-star models such as Starburst99 (Leitherer et al. 2014) and the single-star BPASS models: the binary models predict a broad stellar He IIλ1640 emission line (for constant SF models) not present in single-star models. This feature is detected in all our rest-UV composite spectra; see Section 4. For these reasons, we elect to employ the BPASSv2.2 models over the more commonly used (Bruzual & Charlot 2003, hereafter BC03) solar metallicity models.

The SED fitting procedure, characteristic uncertainties for each SED fit parameter, and comparisons to other SPS models are discussed in Appendix A.

3.2. Attenuation Curves

We fit SEDs to each galaxy, assuming two attenuation curves for the stellar continuum: Calzetti et al. (2000) and SMC. Throughout the paper, we assume these two curves when comparing results, in order to both examine the effects of different assumptions of attenuation curve and place constraints on the most appropriate curve for the majority of high-redshift galaxies.

[6] While galaxies at these redshifts would likely have a rising SFH in reality, we expect the results assuming constant SFHs to be similar (Reddy et al. 2012a). Rising SFHs will be implemented in a future paper.

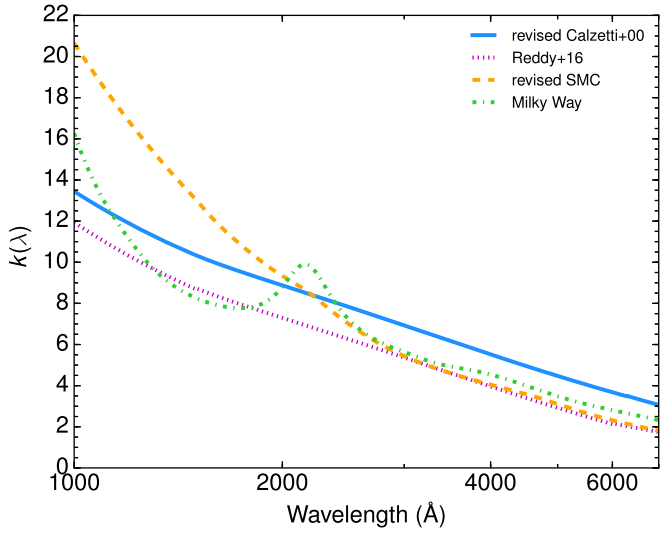

Figure 2. Comparison of attenuation curves discussed in this paper: the Calzetti et al. (2000) starburst attenuation relation, the attenuation curve of Reddy et al. (2016a), the SMC (Gordon et al. 2003), and the Milky Way extinction curve of Cardelli et al. (1989). The revised Calzetti et al. (2000) and SMC curves, used in this paper, include an empirical extension to the far-UV, using the method described in Reddy et al. (2016a).

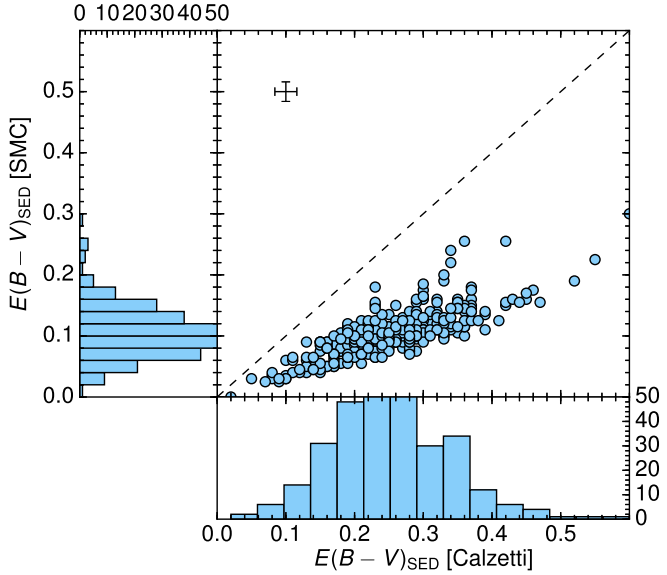

Figure 3. $E(B-V)_{\rm SED}$ assuming the Calzetti et al. (2000) attenuation curve vs. $E(B-V)_{\rm SED}$ assuming the SMC extinction curve, for the 317 galaxies with $>3\sigma$ measurements of BD (including the uncertainties on the slit loss corrections in H and K). Here, all quantities are derived from a BPASSv2.2 $Z_*=0.002$ binary model. SMC predicts a lower $E(B-V)_{\rm SED}$ by a factor of 2.4 on average.

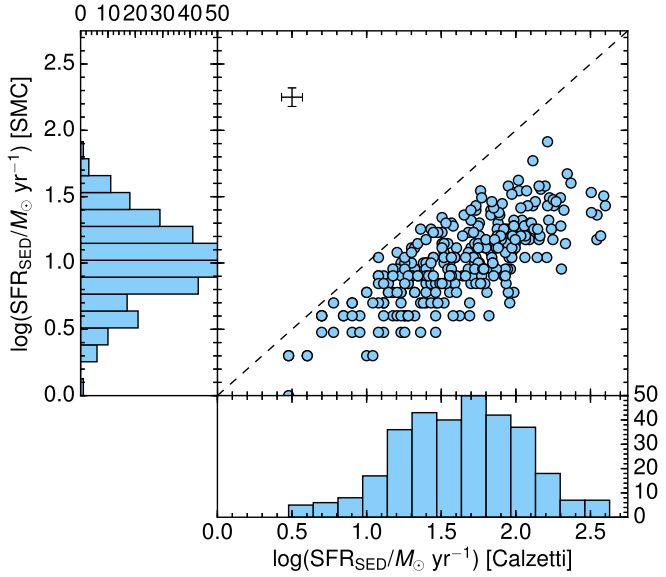

Figure 4. $\rm SFR_{SED}$ assuming the Calzetti et al. (2000) attenuation curve vs. $\rm SFR_{SED}$ assuming the SMC extinction curve, for the 317 galaxies with $>3\sigma$ measurements of BD (including the uncertainties on the slit loss corrections in H and K). Here, all quantities are derived from a BPASSv2.2 $Z_*=0.002$ binary model. SMC predicts a lower $\rm SFR_{SED}$ by 0.50 dex on average.

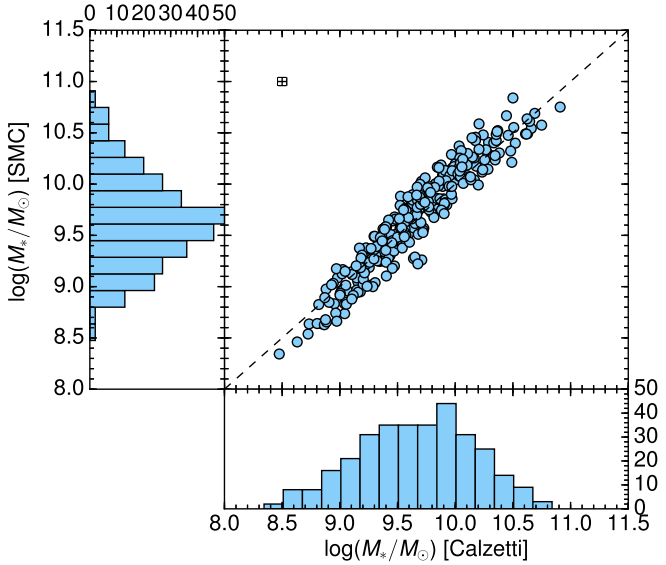

Figure 5. M_* assuming the Calzetti et al. (2000) attenuation curve vs. M_* assuming the SMC extinction curve, for the 317 galaxies with $>3\sigma$ measurements of BD (including the uncertainties on the slit loss corrections in H and K). Here, all quantities are derived from a BPASSv2.2 $Z_*=0.002$ binary model. The stellar masses predicted by both curves are consistent on average.

For the nebular emission lines, we assume the Milky Way curve of Cardelli et al. (1989), with $R_V=3.1$, or SMC for comparison when the continuum attenuation curve is assumed to be SMC.[7] The "SMC" curve used here combines the empirical SMC extinction curve from Gordon et al. (2003, assuming $R_V=2.74$) with an empirical extension to the far-UV using the method described by Reddy et al. (2016a). The version of the Calzetti et al. (2000) curve we use here has also been revised to include an extension to the far-UV using the same method. Similarly, we fit SEDs using an attenuation curve that combines the results of Reddy et al. (2015) based on the MOSDEF survey (Kriek et al. 2015) with a new empirical extension to the far-UV described by Reddy et al. (2016a). The results using this curve are similar to Calzetti et al. (2000), so for simplicity, we discuss only Calzetti et al. (2000) and SMC in this paper. The four curves discussed here are compared in Figure 2.

[7] While the choice of attenuation curve used to correct the stellar continuum has a large effect on the SED-inferred SFRs, it makes very little difference which curve is used to correct nebular emission line ratios, as all the commonly employed curves have a very similar slope and normalization in the optical regime (see Figure 2). Note, however, that the Calzetti et al. (2000) curve has a higher normalization due to the difference in R_V.

Figures 3–5 compare the distributions of $E(B-V)_{\rm SED}$, $\rm SFR_{SED}$, and M_*, for Calzetti et al. (2000) and SMC attenuation. While the inferred stellar masses are consistent within the errors, using SMC results in a lower $E(B-V)_{\rm SED}$ and $\rm SFR_{SED}$ due to the greater degree of attenuation per unit reddening in the UV. On average, the $E(B-V)_{\rm SED}$ inferred for SMC is lower than that inferred for Calzetti et al. (2000) by a factor of 2.4, and the $\rm SFR_{SED}$ is lower by a factor of 3.3, or 0.5 dex.

We find that the SEDs of 38% of galaxies in the sample are better fit by SMC, 16% are better fit by Calzetti et al. (2000), and 46% are comparably fit by either curve within the uncertainty. This result is in contrast to findings in the literature—most previous studies have agreed that the same attenuation curve likely does not apply to every galaxy at high redshift, but have nevertheless argued that one curve or another is more appropriate for the large majority of galaxies at high redshift. The implications of this result are discussed in Section 6; details and example SED fits are given in Appendix A.

3.3. Nebular Reddening and Hα SFR

Nebular reddening $E(B-V)_{\rm neb}$ was calculated from BD using the equation

$$E(B-V)_{\rm neb} = \frac{2.5}{k({\rm H}\beta) - k({\rm H}\alpha)} \log_{10}\left(\frac{\rm BD}{2.86}\right), \quad (1)$$

where $k(\rm H\beta)$ and $k(\rm H\alpha)$ are the values of the attenuation curve evaluated at the wavelengths of Hβ and Hα, respectively; recall that $k(\lambda) = A_\lambda/E(B-V)$.

The attenuation at Hα is

$$A_{\rm H\alpha} = k({\rm H}\alpha)E(B-V)_{\rm neb} = 2.54E(B-V)_{\rm neb} = 5.90\log_{10}\left(\frac{\rm BD}{2.86}\right) \quad (2)$$

when assuming Cardelli et al. (1989) extinction and $R_{\rm V} = 3.1$, or

$$A_{\rm H\alpha} = k({\rm H}\alpha)E(B-V)_{\rm neb} = 2.17E(B-V)_{\rm neb} = 4.95\log_{10}\left(\frac{\rm BD}{2.86}\right) \quad (3)$$

when assuming SMC extinction and $R_{\rm V} = 2.74$. The typical uncertainty on BD, accounting for the errors on the relative slit corrections in H and K, is 14%. Of the 317 $z \sim 2.3$ galaxies studied in this paper, 51 (16% of the sample) have BD < 2.86, the nominal expectation for zero nebular reddening assuming Case B conditions and $T_{\rm e} = 10{,}000$ K. All but eight of these are consistent with BD = 2.86 within 2σ. Galaxies with BD ⩽ 2.86 were assigned $E(B-V)_{\rm neb} = 0$.

SFRs (hereafter $\rm SFR_{H\alpha}$) were estimated using the observed Hα recombination line luminosities, then corrected using either Equation (2) or, in cases where $\rm SFR_{H\alpha}$ was compared to a quantity where continuum attenuation assumes SMC, Equation (3).

To determine the appropriate conversion between Hα luminosity and SFR for each galaxy, we calculated the ionizing photon production rate corresponding to the best-fit SED by integrating the SED up to 912 Å:

$$N({\rm H}^0) = \int_0^{912\text{Å}} \frac{\lambda f_\lambda}{hc} d\lambda. \quad (4)$$

The BPASSv2.2 SEDs are in units of f_λ per $M_\odot$ yr^{-1} of star formation, so the expected $L_{\rm H\alpha}$ per $M_\odot$ yr^{-1} of star formation can then be calculated using the equation from Leitherer & Heckman (1995):

$$L_{\rm H\alpha}({\rm erg\ s^{-1}}) = \frac{1.36N({\rm H}^0)}{10^{12}}\ ({\rm s^{-1}}). \quad (5)$$

In general, an SFR can then be estimated by the following relation, for $t = 10^8$ yr, assuming an IMF upper mass cutoff of 100 $M_\odot$:

$$\log({\rm SFR_{H\alpha}}/M_\odot\ {\rm yr^{-1}}) = \log(L_{\rm H\alpha}/{\rm erg\ s^{-1}}) - C \quad (6)$$

where, for our fiducial BPASSv2.2 $Z_* = 0.002$ model with $t = 10^8$ yr, assuming an IMF upper mass cutoff of 100 $M_\odot$, $C = 41.64$. For comparison, this constant value of 41.64 is 0.34 dex higher than the value of 41.30 from Kennicutt & Evans (2012), once they have been converted to the same IMF. Hα conversion factors for different model assumptions are given in Table 2. The $L_{\rm H\alpha}/\rm SFR$ ratio depends on the spectral shape in the EUV, and when emission line ratios are used to identify models with plausible EUV spectral shapes (as in Steidel et al. 2016) they are the models that produce significantly larger numbers of ionizing photons per $M_\odot$ of star formation. This issue is discussed in Section 6.3.

Also given in Table 2 are SFR calibrations evaluated at $\lambda = 1500$ Å, defined as:

$$\log({\rm SFR_{H\alpha}}/M_\odot\ {\rm yr^{-1}}) = \log(\nu L_\nu/{\rm erg\ s^{-1}}) - C, \quad (7)$$

where νL_ν is evaluated at 1500 Å, as well as values of the ionizing photon production efficiency $\xi_{\rm ion}$:

$$\xi_{\rm ion} = \frac{N({\rm H}^0)}{L_{\rm UV}}\ ({\rm s^{-1}/erg\ s^{-1}\ Hz^{-1}}), \quad (8)$$

where again $L_{\rm UV}$ is measured at 1500 Å. Combined with Equation (5), this means that $\xi_{\rm ion} \propto L_{\rm H\alpha}/L_{\rm UV}$. Although these numbers are not explicitly used in this paper, they are illustrative because $\rm SFR_{SED}$ is primarily sensitive to the non-ionizing UV luminosity, rather than the ionizing photon production rate, because it is derived entirely longward of 912 Å. This can be seen in the fact that the 1500 Å SFR calibrations for the 300 $M_\odot$ and 100 $M_\odot$ BPASSv2.2 models are similar because the non-ionizing UV luminosity per unit SF has very limited IMF dependence.

Figure 6 shows the distribution of BD, $E(B-V)_{\rm neb}$, and $\rm SFR_{H\alpha}$, where $E(B-V)_{\rm neb}$ was calculated from BD assuming a Cardelli et al. (1989) extinction curve.

3.4. Gas-phase Oxygen Abundances

The values of gas-phase oxygen abundance quoted in this paper are inferred using the O3N2 index (O3N2 ≡ log[([O III] λ5008/Hβ)/([N II]λ6585/Hα)]; Pettini & Pagel 2004). Steidel et al. (2014) showed that, compared to the N2 index (N2 ≡ log([N II]λ6585/Hα)) (Pettini & Pagel 2004), oxygen abundances measured from the O3N2 index were less affected by bias and scatter relative to direct $T_{\rm e}$-based measurements of individual KBSS-MOSFIRE galaxies. In this paper, we use

Table 2
Star Formation Rate Calibrations

Model	$\log(L_{H\alpha}/M_\odot\ yr^{-1})$[a]	$\log(\nu L_\nu/M_\odot\ yr^{-1})$ [1500 Å][b]	$\log(\xi_{ion}/[erg\ s^{-1}\ Hz^{-1}])$[c]
BPASSv2.2 300 $M_\odot$ $Z_* = 0.002$	41.78	43.51	25.44
BPASSv2.2 100 $M_\odot$ $Z_* = 0.002$	41.64	43.46	25.35
BPASSv2.2 100 $M_\odot$ $Z_* = 0.004$	41.59	43.46	25.30
BPASSv2.2 100 $M_\odot$ $Z_* = 0.020$	41.35	43.36	25.16
BC03 $Z_* = 0.004$	41.37	43.44	25.10
BC03 $Z_* = 0.020$	41.14	43.40	24.91
Kennicutt & Evans (2012)	41.30	43.35	25.12

Notes. All quantities are corrected to the default BPASS IMF. BPASSv2.2 and BC03 values assume a star formation timescale of $t = 10^{8.0}$ yr.
[a] Conversion factor between Hα luminosity and SFR, as defined by Equation (6).
[b] Conversion factor between UV luminosity at 1500 Å and SFR, as defined by Equation (7).
[c] Ionizing photon production efficiency ξ_{ion}, as defined by Equation (8).

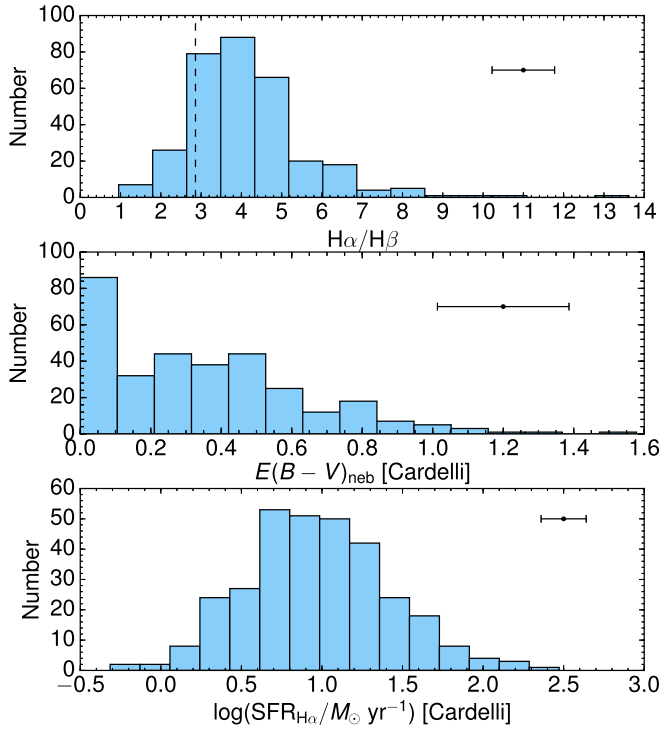

Figure 6. Histogram of Hα/Hβ, $E(B-V)_{neb}$, and $SFR_{H\alpha}$ for the 317 galaxies with $>3\sigma$ measurements of BD. The dashed line denotes the theoretical limit of BD in the case of no dust reddening, BD = 2.86. Galaxies with BD $\leqslant$ 2.86 (13% of the sample) are assigned $E(B-V)_{neb} = 0$. Here, $E(B-V)_{neb}$ and $SFR_{H\alpha}$ assume Cardelli et al. (1989) extinction. The error bars represent the median uncertainty in each quantity.

the recalibration of O3N2 proposed by Strom et al. (2017), based on the sample of extragalactic H II regions compiled by Pilyugin et al. (2012), with an 0.24 dex offset added to place the T_e estimates (based on collisionally excited line ratios) onto the same scale as those measured from recombination lines (Esteban et al. 2014; Steidel et al. 2016).[8]

$$12 + \log(O/H)_{O3N2} = 8.80–0.20\ O3N2. \quad (9)$$

Because [O III]λ5008 and Hβ are close in wavelength and [N II] λ6585 and Hα are also close in wavelength, the ratio O3N2 and thus $12 + \log(O/H)_{O3N2}$ is reddening-independent. An important point made by several authors (e.g., Steidel et al. 2014; Sanders et al. 2016; Strom et al. 2017) is that the "strong-line" metallicity calibrations established in the local universe may not be accurate at high redshift. The locus of the $z \sim 2.3$ KBSS-MOSFIRE sample is offset with respect to similarly-selected $z \sim 0$ galaxies from the Sloan Digital Sky Survey (SDSS) in the log([O III]λ5008/Hβ) versus log([N II]λ6585/Hα) (N2-BPT) plane, likely driven by harder ionizing spectra at fixed nebular O/H (Steidel et al. 2014, 2016; Strom et al. 2017). Additionally, at high redshift, the strong-line ratios become less sensitive to the ionized gas-phase oxygen abundance and more sensitive to the overall spectral shape of the ionizing radiation field produced by massive stars. In practice, this means that the inference of gas-phase metallicity from the O3N2 index is uncertain at high redshift, because O3N2 also tracks excitation. We continue to use O3N2-based inferences of $12 + \log(O/H)$ in this paper, with the caveat that trends of increasing $12 + \log(O/H)_{O3N2}$ may also be interpreted as trends of decreasing excitation.

[8] This offset also makes $(N/O) = (N/O)_\odot$ when $(O/H) = (O/H)_\odot$ for the calibration sample.

4. Inferences from Composite Rest-UV Spectra

As discussed above, we first estimated continuum reddening from SED fitting to broadband photometry. However, many of the SED fit parameters are degenerate with one another. In order to place independent constraints on the relationship between continuum reddening and other galaxy properties, we generated composite rest-UV spectra in equal-number bins of six galaxy properties: $E(B-V)_{SED}$, Hα/Hβ (here converted to $E(B-V)_{neb}$), $12 + \log(O/H)_{O3N2}$, M_*, $SFR_{H\alpha}$, and SFR_{SED}. We then fit SPS models to each stack in order to determine the best-fit combination of Z_* and continuum reddening (hereafter $E(B-V)_{cont}$) as a function of these six parameters. We performed this analysis assuming both Calzetti et al. (2000) and SMC attenuation in order to examine whether the best-fitting attenuation curve systematically varies with galaxy properties.

Composite rest-UV spectra were generated for the subset of 270 galaxies out of 317 with complementary LRIS and MOSFIRE spectra described in Table 1 (hereafter the LRIS +MOSFIRE sample). The stacking technique is described in Appendix B. To fit model spectra to the observed data, we used the far-UV spectra generated by the BPASSv2.2 model suite (Stanway & Eldridge 2018) assuming a constant SFH with an age of 10^8 yr, an upper mass IMF cutoff of 100 $M_\odot$, and binary evolution included. The stellar metallicity Z_* and reddening $E(B-V)_{cont}$ were free parameters in the fitting procedure, and the best-fit combination of Z_* and $E(B-V)_{cont}$ was determined by a χ^2 minimization. Details of the fitting procedure are described in Appendix B.

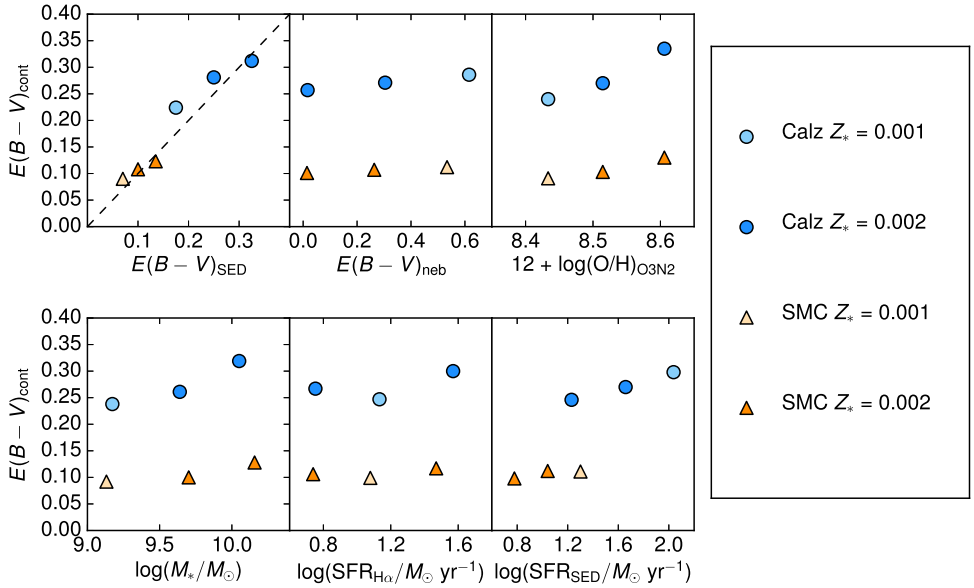

Figure 7. Trends between $E(B-V)_{\rm cont}$ as measured from the stacked rest-UV spectra shown in Figure 16 and the six binned quantities: $E(B-V)_{\rm SED}$, BD (here converted to $E(B-V)_{\rm neb}$), $12+\log({\rm O/H})_{\rm O3N2}$, M_*, ${\rm SFR}_{\rm H\alpha}$, and ${\rm SFR}_{\rm SED}$. The blue circles correspond to model fits assuming the Calzetti et al. (2000) attenuation curve and the orange triangles assume SMC. In both cases, the light-colored points correspond to the spectra fit best by a $Z_*=0.001$ model, and the dark-colored points correspond to those fit best by a $Z_*=0.002$ model. Error bars on $E(B-V)_{\rm cont}$ are smaller than the size of the points and are determined by selecting the range in $E(B-V)_{\rm cont}$ corresponding to $\Delta\chi^2/\nu\sim0.04$ or $\Delta\sigma=1$ (as in Steidel et al. 2016). While $E(B-V)_{\rm cont}$ shows increasing trends with every quantity, the stellar metallicity of the best-fit model is consistently much lower relative to solar than the inferred oxygen abundances, indicating an enhancement of O/Fe.

Figure 7 shows the best-fit values of $E(B-V)_{\rm cont}$ as a function of each of the six binned quantities: $E(B-V)_{\rm SED}$, $H\alpha/H\beta$ (here converted to $E(B-V)_{\rm neb}$), $12+\log({\rm O/H})_{\rm O3N2}$, M_*, ${\rm SFR}_{\rm H\alpha}$, and ${\rm SFR}_{\rm SED}$. Results are shown for both Calzetti et al. (2000) and SMC attenuation. Again, we found that the majority of the stacks did not significantly favor one curve over the other, and the best-fitting curve did not systematically vary with galaxy properties.

The bins in $E(B-V)_{\rm SED}$ served as a test case, to ensure that photometric and spectroscopic fitting results were internally consistent. We expect $E(B-V)_{\rm SED}$ and $E(B-V)_{\rm cont}$ to be strongly correlated, although the correlation might not be 1:1 due to the fact that the stellar metallicity corresponding to $E(B-V)_{\rm cont}$ is allowed to vary freely, whereas the SED fitting fixes the stellar metallicity at $Z_*=0.002$.[9] The best-fit values of $E(B-V)_{\rm cont}$ increase monotonically with increasing $E(B-V)_{\rm SED}$, as expected, and stay very close to the median values of $E(B-V)_{\rm SED}$ in the bins.

We find that all composites are fit best by either a $Z_*=0.001$ model ($Z_*/Z_\odot=0.07$) or a $Z_*=0.002$ model ($Z_*/Z_\odot=0.14$). This is as we might expect based on the analysis from Steidel et al. (2016), who used a similar χ^2 minimization analysis for the "LM1" stack (which contains some of the same galaxy spectra as this sample) and found that models with $Z_*\geqslant0.003$ were strongly disfavored compared to those with $Z_*\leqslant0.002$. Similarly, Strom et al. (2017, 2018) showed, using photoionization modeling, that only binary models with $Z_*\sim0.001$–0.002 were able to reproduce the nebular line ratios observed in most individual $z\sim2.3$ galaxies.

Steidel et al. (2016) and Strom et al. (2017, 2018) also found that the observed nebular emission line ratios require relatively high gas-phase oxygen abundances ($Z_{\rm neb}/Z_\odot\simeq0.5$, or $12+\log({\rm O/H})\simeq8.39$). The apparent discrepancy between Z_* and $Z_{\rm neb}$ can be explained by the fact that the EUV and FUV stellar spectra are controlled primarily by Fe/H, whereas $Z_{\rm neb}$ effectively is the gas-phase O/H. This requires a factor of $\sim$5 enhancement in O/Fe relative to solar that is consistent with the expected yields from core-collapse supernovae (e.g., Nomoto et al. 2006).

Because the ages we infer for the galaxies in our sample are $\sim$50–300 Myr, and the delay timescale for Fe enrichment of the ISM by Type Ia supernovae is $\sim$300–400 Myr, the ISM metallicities in these galaxies (and thus the abundances of the massive stars) are indeed likely dominated by core-collapse supernovae. Rising SFHs, which are expected for galaxies during the period of most rapid growth (Reddy et al. 2012a), can extend the time period over which ISM enrichment remains dominated by core-collapse supernovae. Steidel et al. (2016) argued that, under these conditions, galaxies can reach near-solar gas-phase O/H while Fe abundance remains low. Our result is consistent with this general picture, where stellar metallicity is uniformly low at all values of nebular reddening (Figure 16(b)) and $12+\log({\rm O/H})_{\rm O3N2}$ (Figure 16(c)).

While $E(B-V)_{\rm cont}$ shows a monotonic trend with most of the binned quantities, the strength of the trend varies—the weakest trends are with $E(B-V)_{\rm neb}$ and ${\rm SFR}_{\rm H\alpha}$. In the following section, we explore these relationships for *individual galaxies* using $E(B-V)_{\rm SED}$, which we have argued is an equally good measure of continuum reddening—and we show that the same general trends still hold.

5. Inferences from Individual Galaxies

As discussed in Section 1, the relationship between $E(B-V)_{\rm neb}$ and $E(B-V)_{\rm cont}$ is a contentious topic in the literature. Our aim is to place independent constraints on this relationship by measuring continuum reddening by two different means. In the previous section, we compared $E(B-V)_{\rm neb}$ to $E(B-V)_{\rm cont}$ as measured from SPS model fits to rest-UV composite spectra

[9] We expect $Z_*\sim0.001$–0.002; see below.

Table 3
Spearman Rank-order Correlations

Correlated Quantities[a]	Spearman ρ[b]	Spearman σ[c]
$E(B-V)_{\rm neb}$ [Cardelli] versus $E(B-V)_{\rm SED}$ [Calzetti]	0.15	2.6
$E(B-V)_{\rm neb}$ [SMC] versus $E(B-V)_{\rm SED}$ [SMC]	0.13	2.3
$12+\log({\rm O/H})_{\rm O3N2}$ versus $E(B-V)_{\rm neb}$ [Cardelli]	0.06	1.1
$12+\log({\rm O/H})_{\rm O3N2}$ versus $E(B-V)_{\rm SED}$ [Calzetti]	0.17	3.0
$12+\log({\rm O/H})_{\rm O3N2}$ versus $E(B-V)_{\rm SED}$ [SMC]	0.17	3.0
$E(B-V)_{\rm neb}$ [Cardelli] versus M_* [Calzetti]	0.23	4.2
$E(B-V)_{\rm neb}$ [SMC] versus M_* [SMC]	0.21	3.7
$\rm SFR_{H\alpha}$ [Cardelli] versus $\rm SFR_{SED}$ [Calzetti]	0.24	4.3
$\rm SFR_{H\alpha}$ [SMC] versus $\rm SFR_{SED}$ [SMC]	0.33	6.0

Notes.
[a] Correlations between quantities discussed in Section 5, for individual galaxies, i.e., Figures 8 through 12. The assumed attenuation curves are indicated in brackets.
[b] Spearman rank-order correlation coefficient between each combination of quantities.
[c] Standard deviations from null hypothesis, i.e., no correlation.

in bins of $E(B-V)_{\rm neb}$. Here, we compare $E(B-V)_{\rm neb}$ to $E(B-V)_{\rm SED}$—i.e., continuum reddening as measured from SED fits to *individual* galaxies. We also examine this relationship under different assumptions of attenuation curve. Finally, we compare the correlations between *nebular* reddening, gas-phase oxygen abundance, and M_* to the correlations between *continuum* reddening and the same quantities. Spearman rank-order correlation coefficients for each combination of quantities discussed in the following sections are given in Table 3.

5.1. Relationship between Nebular and Continuum Attenuation

Figure 8 compares $E(B-V)_{\rm SED}$ to $E(B-V)_{\rm neb}$ for two combinations of continuum attenuation curve and nebular extinction curve. The solid lines in Figure 8 represent orthogonal distance regressions fit to the data, which can be used to derive a translation between $E(B-V)_{\rm SED}$ and $E(B-V)_{\rm neb}$, similar to that proposed by Calzetti et al. (2000). With this sample, we find:

$$E(B-V)_{\rm neb,MW} = (1.34\pm0.05)E(B-V)_{\rm SED,Calz} \quad (10)$$

$$E(B-V)_{\rm neb,SMC} = (3.06\pm0.15)E(B-V)_{\rm SED,SMC} \quad (11)$$

assuming either Cardelli et al. (1989) Milky Way extinction and Calzetti et al. (2000) attenuation, or SMC for both lines and continuum. The error bars on the coefficients are the standard deviation of the orthogonal distance regression, and the median scatters about each the best-fit lines (in the $E(B-V)_{\rm neb}$ direction) are 0.20 (Cardelli/Calzetti) and 0.19 (SMC). Spearman rank-order correlation coefficients for both combinations of curves are given in Table 3.

As discussed in Section 1, however, relations between $E(B-V)_{\rm neb}$ and $E(B-V)_{\rm cont}$ are often misinterpreted as relations between the *attenuation* of lines and continuum. However, the latter requires an additional factor of $k(\lambda)$ in addition to what is assumed when deriving $E(B-V)_{\rm neb}$ and $E(B-V)_{\rm cont}$, and it is often the case in the literature that these assumptions are not internally consistent. For clarity, we provide relations between $A_{\rm H\alpha,neb}$, i.e., the attenuation affecting Hα photons emitted via recombination in H II regions, and $A_{\rm H\alpha,cont}$, i.e., the attenuation affecting continuum photons at $\lambda = 6564$ Å:

$$A_{\rm H\alpha,neb}\ [{\rm MW}] = (1.02\pm0.04)A_{\rm H\alpha,cont}\ [{\rm Calz}] \quad (12)$$

$$A_{\rm H\alpha,neb}\ [{\rm SMC}] = (3.06\pm0.15)A_{\rm H\alpha,cont}\ [{\rm SMC}] \quad (13)$$

again assuming either Cardelli et al. (1989) Milky Way extinction and Calzetti et al. (2000) attenuation, or SMC for both lines and continuum.

5.2. Relationship between Reddening and Gas-phase Metallicity

One might expect dust reddening and gas-phase enrichment to be strongly correlated, as metals in the ISM will be depleted onto the same dust grains that attenuate the nebular emission lines—the higher the metal content of the ISM, the more dust grains will be formed (Reddy et al. 2010). Motivated by this picture, the left-hand panel of Figure 9 compares measurements of $E(B-V)_{\rm neb}$ to $12+\log({\rm O/H})_{\rm O3N2}$. For comparison, the left-hand panel of Figure 9 shows $12+\log({\rm O/H})_{\rm O3N2}$ for low-redshift galaxies from SDSS-DR7 (Abazajian et al. 2009, grayscale contours), selected to have detection properties similar to those of KBSS-MOSFIRE (see Strom et al. 2017). Figure 9 shows that, compared to SDSS, the KBSS sample has systematically lower $12+\log({\rm O/H})_{\rm O3N2}$ by 0.21 dex on average. The right-hand panel of Figure 9 compares $12+\log({\rm O/H})_{\rm O3N2}$ with $E(B-V)_{\rm SED}$, where the orange stars are measurements of $E(B-V)_{\rm cont}$ for the stacked rest-UV spectra in bins of $12+\log({\rm O/H})_{\rm O3N2}$ (see Section 4). The measurements of $E(B-V)_{\rm cont}$ for the stacks show good agreement with the median $E(B-V)_{\rm SED}$ in the bins (yellow stars), again demonstrating that SED fitting and SPS fitting to rest-UV spectra provide, on average, consistent estimates of the stellar continuum reddening.

We observe no statistically significant correlation between $12+\log({\rm O/H})_{\rm O3N2}$ and $E(B-V)_{\rm neb}$ (1.1σ; Table 3). However, we do observe a strong correlation between $12+\log({\rm O/H})_{\rm O3N2}$ and $E(B-V)_{\rm SED}$ (3.0σ). While the lack of correlation between $12+\log({\rm O/H})_{\rm O3N2}$ and $E(B-V)_{\rm neb}$ is surprising, for reasons discussed above, the correlation between $E(B-V)_{\rm SED}$ and $12+\log({\rm O/H})_{\rm O3N2}$ may be explained if both the overall shape of the spectrum and the O3N2 line index are sensitive to the shape of the ionizing radiation field produced by the massive stars. This issue is further discussed in Section 6.2.

5.3. Relationship between E(B − V), M_*, and SFR

The left-hand panel of Figure 10 compares measurements of $E(B-V)_{\rm neb}$ to M_*; as before, local galaxies from SDSS-DR7 are shown as grayscale contours for comparison. The median

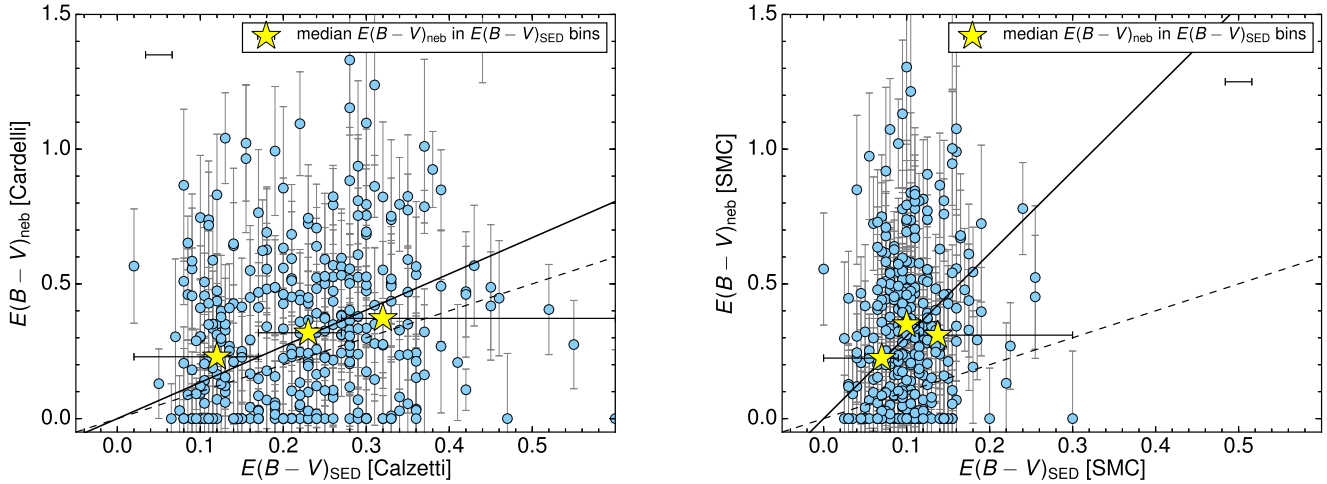

Figure 8. $E(B-V)_{neb}$ vs. $E(B-V)_{SED}$. The solid lines represent orthogonal distance regressions fit to the data (Equation (10)), similar to Calzetti et al. (2000), and the dashed lines represent equal $E(B-V)_{neb}$ and $E(B-V)_{SED}$. Yellow stars are median values of $E(B-V)_{neb}$ in equal-number bins of $E(B-V)_{SED}$, and the bin limits are represented as horizontal error bars. The error bars on $E(B-V)_{neb}$ correspond to a 1σ error in $H\alpha/H\beta$, and the horizontal error bar is the representative error on $E(B-V)_{SED}$ discussed in Appendix A. Left: the SED fitting assumes a Calzetti et al. (2000) attenuation curve and $E(B-V)_{neb}$ assumes a Cardelli et al. (1989) line-of-sight extinction curve. Right: both reddening estimates assume SMC extinction. For both assumed curves, $E(B-V)_{neb}$ is generally greater than $E(B-V)_{SED}$, with large scatter; however, the apparent discrepancy between the two reddening estimates is greater when the SMC curve is assumed.

stellar mass of the KBSS sample is 0.72 dex lower than that of the SDSS sample, and a Kolmogorov–Smirnov (K-S) test revealed that the two samples are drawn from different parent distributions in M_*. However, they are consistent with being drawn from the same parent distribution in $E(B-V)_{neb}$. Both samples show a weak positive correlation between $E(B-V)_{neb}$ and M_*. Thus, at fixed M_*, KBSS galaxies have a greater degree of nebular reddening on average. However, the scatter between the two quantities is large.

The right-hand panel of Figure 10 compares $E(B-V)_{SED}$ to M_*; while these quantities may be degenerate due to the fact that they are both derived from SED fitting, the presence of a correlation is supported by the correlation between $E(B-V)_{cont}$ and M_* (orange stars), which are measured independently. This correlation may be explained by the following argument. M_* is related to the normalization of the model SED relative to the data. $E(B-V)_{SED}$ essentially parameterizes the "shape" of the SED. While the whole spectrum is used for normalization, the matching of the overall shape of the SED is likely to be driven primarily by the shape in the UV, which is also sensitive to parameters such as age and SFH. Because Fe is the dominant source of opacity in stars, higher Fe/H at fixed O/H will make UV spectra intrinsically redder for older galaxies, and thus dust reddening and length of time since the onset of star formation could be degenerate.

5.4. SFR Comparisons

In this paper, SFRs are estimated from both SED fitting (which is primarily sensitive to the UV continuum) and Hα luminosities. If the correct curve is assumed in both the UV and optical regime, and all systematic uncertainties have been accounted for, then these two measures of SFR should agree on average in the case of continuous star formation. Thus, comparisons between $SFR_{H\alpha}$ and SFR_{SED} estimated under different assumptions can be used to place constraints on the most likely combination of physical parameters in the galaxy. The free parameters in this analysis are the continuum attenuation curve, the nebular extinction curve, and the SPS model used for both SED fitting and converting Hα luminosities into SFRs (see Section 3). The latter encodes information about binarity, the IMF, and the stellar abundance of Fe. While we have thus far only used the BPASSv2.2 SPS models in SED fitting, in this section we compare $SFR_{H\alpha}$ to SFR_{SED} assuming both the BPASSv2.2 low-metallicity, binary models and the more commonly used Bruzual & Charlot (2003) single-star, solar metallicity models. For each model, we then compare SFRs, assuming two different combinations of extinction/attenuation curves, in order to constrain the most appropriate combination of SPS model and attenuation curve.

Figure 11 compares $SFR_{H\alpha}$ to SFR_{SED} for the Bruzual & Charlot (2003) $Z_* = 0.020$ models, assuming either Calzetti et al. (2000) attenuation and Cardelli et al. (1989) extinction (left), or SMC for both lines and continuum (right). Also shown in Figure 12 are orthogonal distance regression lines fit to the data, and median values of $SFR_{H\alpha}$ in bins of SFR_{SED}. Using the SMC extinction curve results in values of $\log(SFR_{SED})$ that are offset from $\log(SFR_{H\alpha})$ by a factor of 1.3, whereas using Cardelli et al. (1989) extinction and Calzetti et al. (2000) attenuation results in consistent SFRs on average.

Conversely, Figure 12 compares the same quantities, but instead for the BPASSv2.2 $Z = 0.002$ binary models. In this case, using the Calzetti et al. (2000) curve results in values of $\log(SFR_{SED})$ that are offset from $\log(SFR_{H\alpha})$ by a factor of 1.3, whereas using the SMC curve results in consistent SFRs on average. In all cases, the default BPASS IMF has been assumed, and Hα luminosities have been converted to SFRs by integrating the ionizing portion of the best-fit SED, as described in Section 3.3.

Compared to the BPASSv2.2 $Z_* = 0.002$ binary models, the BC03 $Z_* = 0.020$ models predict values of $SFR_{H\alpha}$ that are 0.5 dex higher on average, once the differences in IMF have been accounted for. SFR_{SED} assuming the BPASS models is higher than that predicted by BC03 $Z = 0.020$ by 0.12 dex, also accounting for differences in IMF.

On the other hand, when the same SED model is assumed, changing the continuum attenuation curve from Calzetti et al. (2000) to SMC lowers SFR_{SED} by 0.69 dex on average, and changing the nebular extinction curve from Cardelli et al. (1989)

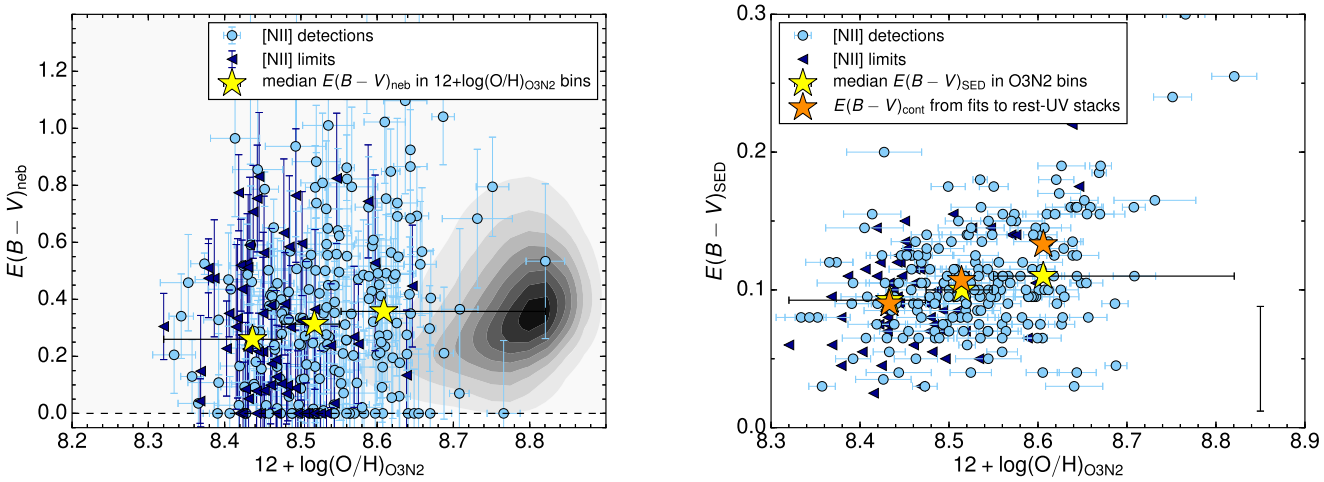

Figure 9. Left: $E(B-V)_{neb}$ vs. 12 + log(O/H)$_{O3N2}$. Dark blue triangles represent 2σ upper limits in [N II]. Yellow stars represent the median measurements of the individual spectra in equal-number bins of 12 + log(O/H)$_{O3N2}$. The grayscale contours represent the locus of similarly selected SDSS galaxies (Strom et al. 2017). Right: $E(B-V)_{SED}$ vs. 12 + log(O/H)$_{O3N2}$, assuming the SMC extinction curve. Orange stars are measurements of $E(B-V)_{cont}$ for stacks of rest-UV spectra in bins of 12 + log(O/H)$_{O3N2}$, and yellow stars are median values of $E(B-V)_{SED}$ in the same bins. Bin limits are shown as black error bars. While we find no significant correlation between 12 + log(O/H)$_{O3N2}$ and $E(B-V)_{neb}$, 12 + log(O/H)$_{O3N2}$ and $E(B-V)_{SED}$ are correlated at 3.0σ significance. Additionally, KBSS galaxies have a lower 12 + log(O/H)$_{O3N2}$ than SDSS galaxies by 0.21 dex on average.

to SMC lowers SFR$_{H\alpha}$ by 0.06 dex on average. Thus, changing the combination of assumptions from BC03 $Z_* = 0.020$ models with Calzetti et al. (2000) attenuation and Cardelli et al. (1989) extinction to BPASSv2.2 $Z_* = 0.002$ models with SMC applied to both lines and continuum lowers SFR$_{SED}$ by 0.57 dex and SFR$_{H\alpha}$ by 0.56 dex. This can be seen clearly in Figures 11 and 12; differences in attenuation curve cancel out differences in SED model. In order to break this degeneracy and determine the most applicable attenuation relation for our sample, independent constraints on the best-fit SED model are needed. This issue is further discussed in Section 6.3.

6. Discussion

6.1. Comparison between Nebular and Continuum Reddening

Although the data in Figure 8 indicate a weak correlation between the reddening toward the ionized nebulae and the stellar continuum, the most obvious feature of Figure 8 is the large scatter between the two quantities. In particular, galaxies with $E(B-V)_{neb} = 0$ (which is defined here as BD $\leqslant 2.86$) span the full range of $E(B-V)_{SED}$. Similarly, the measurements of $E(B-V)_{cont}$ for stacked spectra in bins of BD show only a very weak trend, suggesting that nebular reddening is nearly independent of UV continuum reddening.

This relationship between $E(B-V)_{neb}$ and $E(B-V)_{cont}$ is intriguing because previous studies have reached different conclusions. For example, Steidel et al. (2016) found that the best-fit $E(B-V)_{cont}$ for a stack of 30 $z \sim 2.3$ galaxies with high-quality rest-UV and rest-optical spectra was consistent with the median $E(B-V)_{neb}$ of the individual galaxies contributing to the stack. They suggested that the similarity between these two quantities implies that the nebular emission lines are powered by the same massive stars that are responsible for the far-UV continuum, and thus there is not likely to be a significant population of dust-obscured massive stars contributing to the nebular emission line luminosities but not the far-UV continuum. We find that, with the Calzetti et al. (2000) attenuation curve and Cardelli et al. (1989) extinction curve (similar to the combination of curves employed by Calzetti et al. (2000)), $E(B-V)_{neb} = 1.34E(B-V)_{SED}$ on average, in contrast to the factor of 2.27 between $E(B-V)_{neb}$ and $E(B-V)_{cont}$ proposed by Calzetti et al. (2000) for local starburst galaxies. When the SMC curve is applied to both lines and continuum, we find that $E(B-V)_{neb} = 3.06E(B-V)_{SED}$, which is merely due to the steeper slope of the SMC curve in the UV relative to the Calzetti et al. (2000) curve. This coefficient, however, should not be directly compared to that proposed by Calzetti et al. (2000), as it assumes a different combination of extinction/attenuation curves.

At low redshift, the discrepancy between nebular and continuum color excess is usually attributed to increased dust covering fractions surrounding H II regions; i.e., the youngest stars remain in undissipated parent birth clouds (Calzetti et al. 1994; Charlot & Fall 2000). However, this picture does not explain the significant fraction of galaxies in the KBSS sample for which $E(B-V)_{SED} > E(B-V)_{neb}$.

Additionally, scatter in the relationship between $E(B-V)_{neb}$ and $E(B-V)_{cont}$ may be due to variations in the dust attenuation curve from galaxy to galaxy. It is unlikely that the same attenuation curve applies to every galaxy in our sample, or even every galaxy in a bin of some observed quantity. Theoretical work has suggested that observed variations in the IRX-β relation may be attributed to variations in the dust attenuation curve due to differences in grain composition, as well as stellar population age, dust temperature, and geometry of the dust distribution (e.g., Granato et al. 2000; Popping et al. 2017; Narayanan et al. 2018). Indeed, we find that the same curve cannot be applied to every galaxy in our sample. While 38% of galaxies in our sample have SEDs that are fit best by the SMC curve, 16% are fit best by the Calzetti et al. (2000) curve, and the remainder do not favor either curve within the uncertainty (although the majority of these are fit nominally better by SMC).

6.2. Correlations with Gas-phase Metallicity and Stellar Mass

Figure 9 shows that local galaxies have a higher gas-phase metallicity (and/or lower excitation) at the same $E(B-V)_{neb}$ than high-redshift galaxies. This is consistent with the well-studied offset in the mass–metallicity relation (MZR)

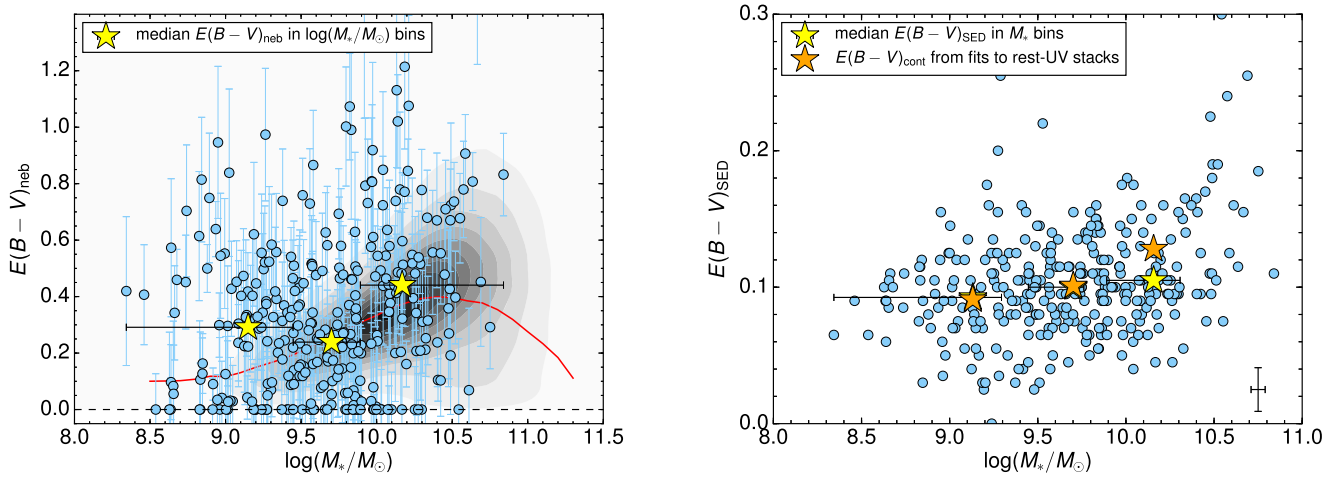

Figure 10. Left: $E(B-V)_{neb}$ vs. M_* inferred from SED fits assuming a BPASSv2.2 $Z_* = 0.002$ continuous star formation model with SMC extinction. The grayscale contours represent the locus of similarly selected SDSS galaxies, and the solid red curve represents the median $E(B-V)_{neb}$ in bins of M_*. The KBSS and SDSS galaxies are consistent with being drawn from the same parent distribution in $E(B-V)_{neb}$, but KBSS galaxies are offset to lower stellar masses; thus, the degree of reddening at fixed stellar mass is higher on average in KBSS galaxies. Right: $E(B-V)_{SED}$ vs. M_*, where both quantities have been inferred from SED fits assuming a BPASSv2.2 $Z_* = 0.002$ continuous star formation model with SMC extinction. The yellow stars represent the median values of $E(B-V)_{SED}$ in equal-number bins of M_*, and the orange stars are measurements of $E(B-V)_{cont}$ from stacks of rest-UV spectra in the same bins. Bin limits are shown as black error bars. As in Figure 9, the trends with continuum reddening are stronger than the trend with nebular reddening.

(Tremonti et al. 2004; Erb et al. 2006; Mannucci et al. 2010; Zahid et al. 2011; Steidel et al. 2014) at high redshift, such that high-redshift galaxies have lower metallicity at fixed M_*.

A number of studies (e.g., Reddy et al. 2010; Heinis et al. 2014; Oteo et al. 2014; Álvarez-Márquez et al. 2016; Bouwens et al. 2016) have noted correlations between continuum dust obscuration and M_*; we find such a correlation for the KBSS sample as well (Figure 10). As discussed above, however, this may alternately be explained by the fact that $E(B-V)_{SED}$, which parameterizes the overall shape of the SED, is also sensitive to age and SFH, both of which are linked to stellar mass.

Other studies have found a redshift-independent relationship between *nebular* attenuation and stellar mass; Domínguez et al. (2013) found, using stacked WFC3 grism spectra of galaxies at intermediate redshift ($0.75 \leqslant z \leqslant 1.5$), that these galaxies have a similar BD at fixed stellar mass as SDSS galaxies (within the errors). We find that there is a statistically significant positive correlation between M_* and $E(B-V)_{neb}$. Although the scatter in this relationship is large, $E(B-V)_{neb}$ is higher on average for KBSS galaxies than SDSS galaxies at fixed stellar mass.

That there is an apparent decrement observed in the stellar mass–metallicity relation (with higher-z galaxies having less chemical enrichment at fixed stellar mass) but no difference in the stellar mass-reddening relation (Figure 10) may at first seem puzzling, as metal and dust content are thought to track one another in galaxies' ISM. However, if dust and metals are produced in the same way at all redshifts, then the true implication of lower gas-phase metallicity in high-z galaxies is that they should have lower dust-to-gas ratios than low-z galaxies at fixed stellar mass. At the same time, galaxies at $z \sim 2$–3 are known to have significantly higher total gas fractions (e.g., Daddi et al. 2008; Tacconi et al. 2010), which may ultimately result in larger dust column densities despite these lower dust-to-gas ratios. There are also additional confounding factors, including how dust grain composition changes with metallicity, and as a result, likely with redshift as well.

Interestingly, we have found (Section 5.2) that the correlation between stellar continuum reddening $E(B-V)_{cont}$ and (reddening-independent) $12 + \log(O/H)_{O3N2}$ is much stronger than that between nebular reddening $E(B-V)_{neb}$ and $12 + \log(O/H)_{O3N2}$ (Figure 9; Table 3). These trends could be explained if $E(B-V)_{SED}$ is a better tracer of gas-phase abundances and/or excitation than $E(B-V)_{neb}$. Several authors (e.g., Steidel et al. 2014; Sanders et al. 2016; Strom et al. 2017) have noted that, at high redshift, line ratios such as O3N2 become less sensitive to gas-phase oxygen abundance and more sensitive to the overall spectral shape of the ionizing radiation field produced by massive stars. Thus, the stronger correlation between $12 + \log(O/H)_{O3N2}$ and $E(B-V)_{SED}$ may be induced because both quantities are closely tied to the spectral shape of the ionizing radiation field produced by the massive stars, which depends on the stellar abundance of Fe.

6.3. SFR Comparisons

Figures 11 and 12 show that the combination of Calzetti et al. (2000) attenuation for the stellar continuum and Cardelli et al. (1989) Galactic extinction for the nebular emission lines produces consistent Hα-based and SED-based SFRs when the BC03 $Z = 0.020$ single-star models are used, as in Steidel et al. (2014). When the BPASSv2.2 $Z = 0.002$ binary models are used, SMC produces consistent SFRs. Perhaps most importantly, we have used the conversion factors from Hα luminosity to SFR that are internally consistent with each SPS model, as described in Section 3. In the case of the BPASSv2.2 $Z = 0.002$ binary models, this has the effect of lowering $SFR_{H\alpha}$ by $\sim$0.35 dex relative to the canonical conversion of Kennicutt & Evans (2012).

As mentioned in Section 3.2, the SEDs of 46% of the sample do not significantly favor either Calzetti et al. (2000) or SMC within the uncertainty. Similarly, while the BPASS models provide a better fit than BC03 for the majority of the sample, 33% do not significantly favor either model within the uncertainty. Thus, the SED fitting alone is not able to constrain either the most appropriate dust attenuation curve or the most

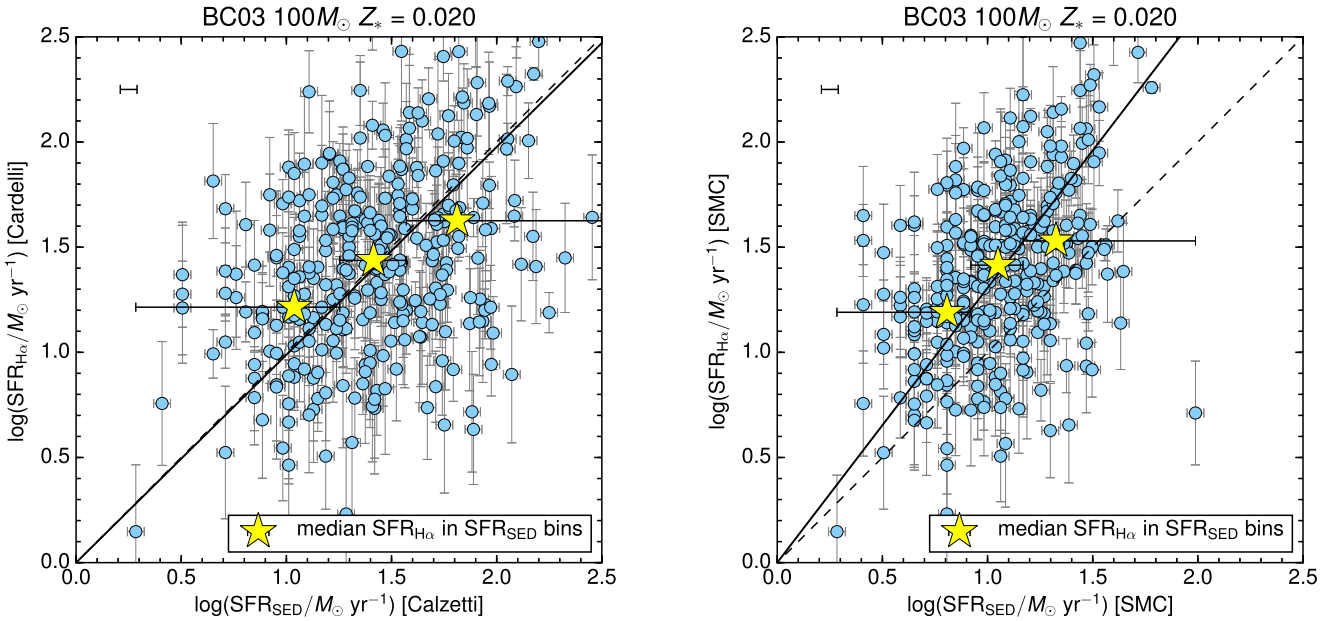

Figure 11. Comparison of star formation rates estimated from SED fitting (SFR_{SED}) to those based on the Hα luminosity ($SFR_{H\alpha}$), for the Bruzual & Charlot (2003) model with $Z_* = 0.020$. The solid lines are orthogonal distance regression lines, and the dashed lines represent equal SFRs. Yellow stars are median vales of $SFR_{H\alpha}$ in equal-number bins of SFR_{SED}, and bin limits are represented as horizontal error bars. Left: the SED fitting assumes a Calzetti et al. (2000) attenuation curve and the Hα measurements assume a Cardelli et al. (1989) line-of-sight extinction curve. Right: both the SED fitting and the Hα measurements assume SMC extinction. Using the SMC extinction curve results in values of $\log(SFR_{SED}$ that are offset from $\log(SFR_{H\alpha})$ by a factor of 1.3, whereas using Cardelli et al. (1989) extinction and Calzetti et al. (2000) attenuation results in consistent SFRs on average.

appropriate SPS model. Indeed, Figure 11 appears to indicate that the combination of Calzetti et al. (2000) attenuation, Cardelli et al. (1989) extinction, and the single-star, solar metallicity BC03 models is a reasonable combination of assumptions, and this is what has been assumed by nearly all previous studies.

However, the BPASSv2.2 $Z_* = 0.002$ models are more consistent with observations than the $Z_* = 0.020$ BC03 models, in that they are better able to simultaneously match the rest-UV continuum, stellar and nebular lines, and rest-optical nebular emission lines. Thus, we argue that the agreement between SFRs when the single-star models are used is likely to be coincidental rather than an indication that these models are an accurate representation of the conditions at high redshift. When the BPASSv2.2 $Z_* = 0.002$ model and corresponding Hα-to-SFR conversion is used, the SMC curve produces consistent SFRs on average, and so we argue that it is the most appropriate attenuation curve for the majority of KBSS galaxies, in agreement with what has been found in several recent studies (e.g., Capak et al. 2015; Bouwens et al. 2016; Koprowski et al. 2016; Reddy et al. 2018).

The large scatter in $SFR_{H\alpha}$ with respect to SFR_{SED} could be explained if the same Hα/SFR conversion factor does not apply to every galaxy in our sample. We show in Table 2 that $L_{H\alpha}$/SFR varies by $\sim$0.5 dex among SPS models, whereas νL_ν/SFR [1500 Å] only varies by $\sim$0.1 dex. $L_{H\alpha}$/SFR is determined by the EUV spectrum of the ionizing stars, which is very sensitive to stellar metallicity (i.e., Fe/H), upper mass IMF cutoff, and binarity. Similarly, Shivaei et al. (2018) found an intrinsic scatter of 0.28 dex in the distribution of the ionizing photon production efficiency ξ_{ion} (which is directly proportional to the $L_{H\alpha}/L_{UV}$ ratio) for galaxies in the MOSDEF survey. They conclude that variations in ξ_{ion} cannot be solely explained by object-to-object variations in the dust attenuation curve; rather, the scatter is affected by stellar population properties such as variations in IMF and stellar metallicity.

We have argued that, on average, the EUV spectra of high-redshift galaxies should look very different from their local counterparts, because the best-fitting SPS models are those characterized by subsolar Fe/H. For individual galaxies, though, there is a wide range of possibilities, and we do not know a priori the intrinsic shape of the EUV spectra, and thus $L_{H\alpha}$/SFR. It may simply be the case that, without firm knowledge of the massive stellar population properties in each galaxy, Hα can only accurately predict SFRs *on average*, and it is a stochastic SFR indicator across the galaxy population.

One potential caveat is that variations between Hα and UV-based SFRs are frequently attributed to "bursty" star formation (e.g., Weisz et al. 2012; Kauffmann 2014; Shivaei et al. 2016; Smit et al. 2016). It is often asserted that the Hα flux traces SFR over $\approx$10 Myr timescales and the UV continuum flux traces SFR over $\approx$200 Myr timescales (Kennicutt & Evans 2012), in which case a galaxy with a heightened Hα/UV flux ratio may have had a short burst of star formation within the last 10 Myr (Sparre et al. 2017). This effect could explain some of the scatter in Figure 12, given that SFR_{SED} is predominantly determined by the UV spectrum and its slope. However, binary stars can significantly extend the timescales over which ionizing photons are produced (Eldridge et al. 2017), and for the galaxies in our sample, we do not expect significant fluctuations in SFR on timescales shorter than $\sim$30 Myr, the typical central dynamical timescale; note also that the SEDs and FUV spectra are fit well by models with constant SFHs with a typical timescale of 10^8 yr. Even in a scenario where bursts were important, we might expect to see a $SFR_{H\alpha}/SFR_{SED}$ ratio that was systematically elevated, which is not the case, at least for the fiducial BPASS model employed in this paper.

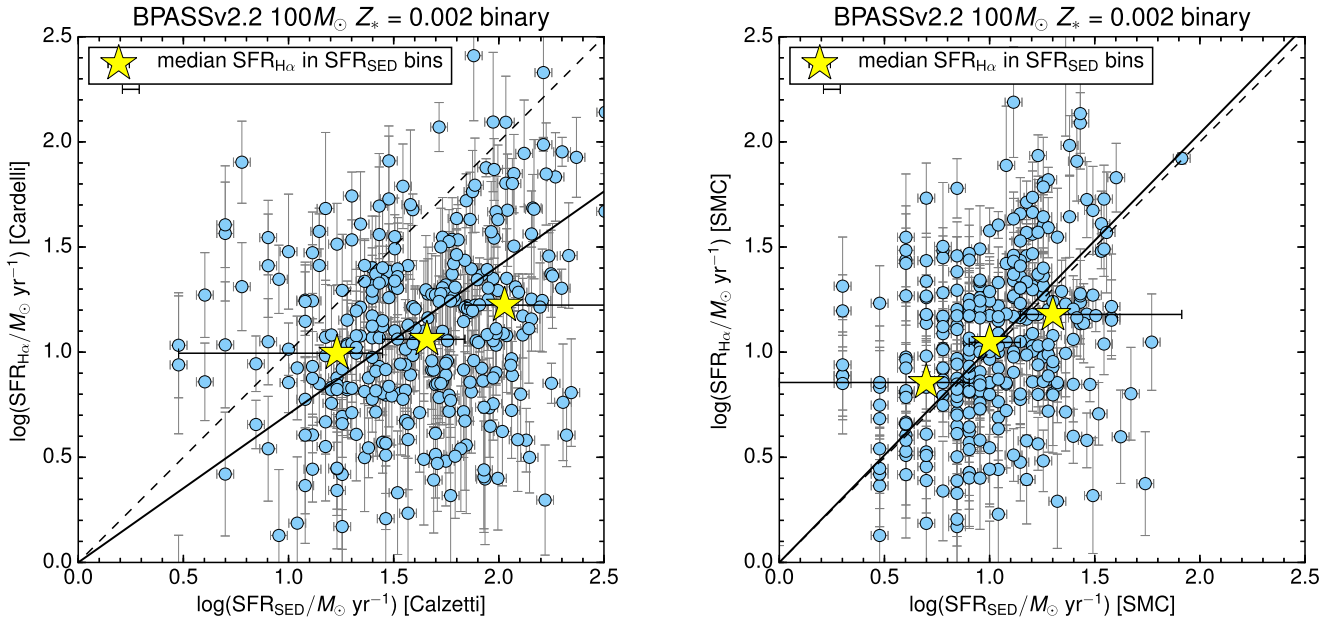

Figure 12. Comparison of star formation rates estimated from SED fitting (SFR_{SED}) to those based on the Hα luminosity ($SFR_{H\alpha}$), for the fiducial model used in this work, BPASSv2.2 $Z_* = 0.002$ with binaries included. The solid lines are orthogonal distance regression lines, and the dashed lines represent equal SFRs. Yellow stars are median vales of $SFR_{H\alpha}$ in equal-number bins of SFR_{SED}, and bin limits are represented as horizontal error bars. Left: the SED fitting assumes a Calzetti et al. (2000) attenuation curve and the Hα measurements assume a Cardelli et al. (1989) line-of-sight extinction curve. Right: both the SED fitting and the Hα measurements assume SMC extinction. Using the Calzetti et al. (2000) curve results in values of $\log(SFR_{SED})$ that are offset from $\log(SFR_{H\alpha})$ by a factor of 1.3, whereas using the SMC curve results in consistent SFRs on average.

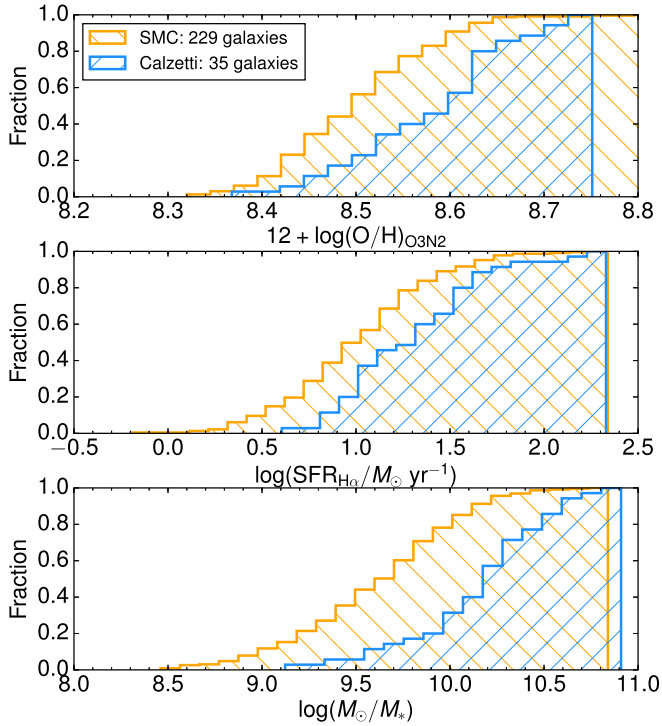

Figure 13. Cumulative histograms of $12 + \log(O/H)_{O3N2}$, $SFR_{H\alpha}$, and M_* for the 16% of galaxies with SEDs fit best by the Calzetti et al. (2000) curve (blue) and the remainder of the sample with SMC applied (orange). Note that the former two quantities are independent of the assumed continuum attenuation curve, and we have shown in Figure 5 that, while the latter quantity requires an assumption of attenuation curve, it is nearly independent of this choice (see Figure 5).

Additionally, while the SMC curve comes the closest to producing consistent SFRs, and it provides the best fit to the SEDs of many of the galaxies in the sample, it may not be the most appropriate attenuation curve for every galaxy. As discussed in Section 3.2, 16% of galaxies in the sample are fit better by Calzetti et al. (2000) within the uncertainties, and 46% of galaxies are comparably fit by either curve.

Interestingly, the subset of galaxies fit better by the Calzetti et al. (2000) curve displays unique properties. A K-S test indicates that these galaxies and the remainder of the sample are drawn from different parent distributions in $12 + \log(O/H)_{O3N2}$ (3.2σ), $SFR_{H\alpha}$ (2.8σ), and M_* (7.0σ). Histograms of these three properties for the subsample fit best by Calzetti et al. (2000) and the remainder of the sample are shown in Figure 13. Thus, it may be the case that this subsample is a population of galaxies distinct from the majority. The detailed properties of the most massive galaxies in the KBSS sample will be explored in a future paper.

7. Summary and Conclusions

We have presented an analysis of a sample of high-quality near-IR (rest-optical) spectra of 317 galaxies at $2.0 \leqslant z \leqslant 2.7$ obtained as a part of KBSS-MOSFIRE (Steidel et al. 2014; Strom et al. 2017) in combination with complementary deep optical (rest-UV) spectra obtained with Keck/LRIS for 270 of these galaxies. We have estimated $E(B-V)_{neb}$ from the BD and continuum attenuation from SED fits to broadband photometry [$E(B-V)_{SED}$] as well as from stellar spectral synthesis model fits to composite rest-UV spectra [$E(B-V)_{cont}$] in bins of $E(B-V)_{neb}$, $12 + \log(O/H)_{O3N2}$, M_*, $SFR_{H\alpha}$, and SFR_{SED}. We compared nebular and continuum estimates of dust reddening to each other and to gas-phase O/H, M_*, and SFR. Finally, we compared Hα and SED-based estimates of SFR. Our conclusions are as follows:

1. $E(B-V)_{neb}$ is correlated with $E(B-V)_{SED}$ for individual galaxies, albeit with large scatter, and there is generally larger reddening toward line-emitting regions.

Fits of BPASSv2.2 stellar spectral synthesis models to composite rest-UV spectra in bins of $E(B-V)_{\rm neb}$ confirm that $E(B-V)_{\rm cont}$ is also correlated with $E(B-V)_{\rm neb}$. We find that, when the SMC curve is applied to both lines and continuum, the discrepancy between $E(B-V)_{\rm neb}$ and $E(B-V)_{\rm SED}$ is larger on average than when the Calzetti et al. (2000) curve is applied to the continuum and the Cardelli et al. (1989) curve is applied to the nebular lines, due to the fact that the SMC curve is much steeper than the Calzetti et al. (2000) curve in the UV but is similar to the Cardelli et al. (1989) Milky Way extinction curve in the optical. As has been discussed in the literature, the relationship between nebular and continuum reddening depends on the details of the attenuation curves used to derive those two quantities. Furthermore, the relationship between nebular and continuum *attenuation* requires additional assumptions of attenuation curves that must be consistent with what has been assumed when deriving $E(B-V)$. Finally, we argue that, due to the large scatter between $E(B-V)_{\rm neb}$ and $E(B-V)_{\rm cont}$, constant factors translating $E(B-V)_{\rm neb}$ to $E(B-V)_{\rm cont}$ (such as that proposed by Calzetti et al. 2000) should be used with caution.

2. $E(B-V)_{\rm neb}$ is not strongly correlated with gas-phase O/H measured from the O3N2 index, which is also sensitive to the shape of the radiation field from the massive stars ionizing the nebulae (e.g., Steidel et al. 2014, 2016; Strom et al. 2017). Relative to local galaxies from SDSS, KBSS galaxies are offset by $\Delta\log({\rm O/H}) = 0.21$ dex toward lower inferred gas-phase oxygen abundance. The relationship between $E(B-V)_{\rm neb}$ and M_* is offset such that $z\sim2.3$ galaxies have greater nebular reddening at a fixed stellar mass than $z\sim0$ galaxies. We interpret the behavior as a natural consequence of lower dust/gas ratios but much higher gas fractions at high redshift.
3. We find that the *continuum* reddening measured from the far-UV spectra is more strongly correlated with the inferred ionized gas-phase O/H (measured using the dust-insensitive O3N2 index) than the nebular reddening measured from the BD toward the same H II regions. The strength of this correlation may be due to the fact that both the O3N2 index, used to measure $12+\log({\rm O/H})_{\rm O3N2}$, and the UV spectral slope, used to measure $E(B-V)_{\rm cont}$, are sensitive to the shape of the ionizing radiation field produced by the massive stars.
4. The use of the Calzetti et al. (2000) attenuation curve in SED fitting produces inconsistent values of $\rm SFR_{SED}$ and $\rm SFR_{H\alpha}$ for all but the highest-$\rm SFR_{H\alpha}$ galaxies when the BPASSv2.2 $Z=0.002$ binary star models and corresponding conversion factors from Hα luminosity to SFR are assumed, which several authors have found is best able to reproduce the observed constraints at high redshift. In contrast, the SMC curve produces consistent SFRs on average, and nominally the best fit to the full SEDs of the majority of the sample, and we argue that SMC is the most appropriate attenuation for the majority of the sample (except for the highest-mass galaxies). The large observed scatter between $\rm SFR_{H\alpha}$ and $\rm SFR_{SED}$ may be plausibly explained by variations in the intrinsic EUV–FUV spectra that are not fully accounted for with standard assumptions.

We emphasize that many of the relations between quantities involving continuum and nebular dust corrections depend sensitively on the details of the assumed continuum attenuation curve. In particular, the SMC curve predicts significantly smaller values of reddening and SFR than the "grayer" Calzetti et al. (2000) curve, and it provides a better fit for many of the galaxies in our sample at $z\sim2.3$. However, a non-negligible fraction is better fit by the Calzetti et al. (2000) attenuation curve, and for these galaxies, the application of the SMC curve would lead to severe underestimates of reddening and SFR. Thus, care must be taken when selecting the most appropriate attenuation curve for a given galaxy at high redshift, and it generally is not a good assumption that the same attenuation curve applies to every galaxy at high redshift.

Perhaps just as importantly, due to large intrinsic variations in $L_{\rm H\alpha}/L_{\rm UV}$ modulated by stellar metallicity, IMF, and the importance of binaries, it is unlikely that the same conversion factor between Hα luminosity and SFR applies to every galaxy at high redshift. We argue that Hα-based SFRs are highly stochastic and therefore remain a significant source of systematic errors in estimating SFRs of high-redshift galaxies.

The authors thank Max Pettini and the anonymous referee for helpful comments. This work has been supported in part by the NSF through grants AST-0908805 and AST-1313472 (CCS, RLT, ALS), by the JPL President-Director Fund (CCS, RLT), by the Professor Wallace L. W. Sargent Graduate Fellowship (RLT) and the Troesh Family Distinguished Scholars Fund (also RLT), and by an Alfred P. Sloan Research Fellowship (NAR). Finally, the authors wish to recognize and acknowledge the significant cultural role and reverence that the summit of Maunakea has within the indigenous Hawaiian community. We are privileged to have the opportunity to conduct observations from this mountain.

Appendix A
SED Fitting

A.1. Fitting Procedure

The SED fitting uses reddened BPASSv2.2 models (Stanway & Eldridge 2018), assuming a constant SFH and a minimum allowed age of 50 Myr. The model SED at each age is redshifted using its measured nebular redshift $z_{\rm neb}$, reddened from $E(B-V)=0$–0.6 in steps of 0.01 (or $E(B-V)=0$–0.3 in steps of 0.005 if the SMC attenuation curve is assumed), and attenuated blueward of rest frame 1216 Å by IGM opacity using Monte Carlo modeling. The best-fit normalization of the model at a given age and reddening step is determined by minimizing χ^2 with respect to the observed photometry, and this normalization determines the SFR and stellar mass. The best-fit combination of age and reddening is then taken to be that which minimizes the overall χ^2. This procedure is repeated for each attenuation curve, and we compare the results assuming different curves throughout this work.

The default BPASSv2.2 models do not include the contribution from the nebular continuum emission. As in Figure 3 of Steidel et al. (2016), we calculated this contribution relative to the stellar continuum by using the photoionization models that produced the best matches to the observed nebular spectra. This contribution was then added to the BPASSv2.2 models before fitting them to the data. The effect of including the nebular continuum is to make

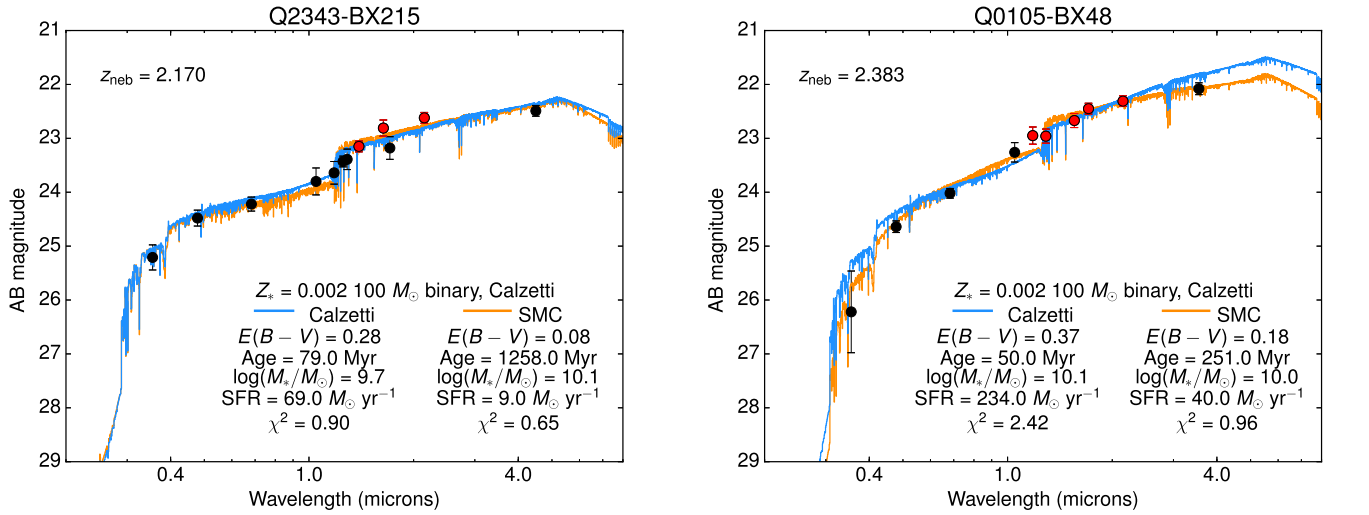

Figure 14. Example SEDs for the galaxies Q2343-BX215 (left; $z_{neb} = 2.170$) and Q0105-BX48 (right; $z_{neb} = 2.383$). Photometric points are shown in black, and red points are those that have been corrected for the emission line contribution. BPASSv2.2 SEDs are shown for the Calzetti et al. (2000) (blue) and SMC (orange) attenuation curves. In the case of Q2343-BX215, both curves give an equally good fit, and while the inferred stellar masses are similar, SMC predicts an older age, lower $E(B-V)_{SED}$, and lower SFR. For Q0105-BX48, however, SMC provides a much better fit.

the total continuum slightly redder than the stellar continuum only, thus requiring slightly lower values of $E(B-V)_{SED}$ to match the data, by 5% on average.

A.2. Fit Parameters and Characteristic Uncertainties

We estimated a characteristic uncertainty on the SED fit parameters by perturbing each photometric point for each galaxy in the sample 100 times within 1σ, and fitting SEDs to each perturbation using each attenuation curve. We found that the average 68% confidence intervals for each parameter were: ± 0.016 dex for $E(B-V)_{SED}$, $[-0.07, +0.09]$ dex for $\log(t/\mathrm{yr})$, $[-0.07, +0.06]$ dex for $\log(\mathrm{SFR}_{SED}$, and ± 0.04 dex for $\log(M_*)$. We found that 46% of the galaxies in the sample were fit equally well by both Calzetti et al. (2000) and SMC within the uncertainty, which we define as the average 68% confidence interval on χ^2 for the 100 iterations of the bootstrap.

The left-hand panel of Figure 14 shows example SED fits for one such galaxy, Q2343-BX215 (left; $z_{neb} = 2.17$). Both curves gave similar values of χ^2 in this case, and while the inferred stellar masses are similar for both curves, SMC predicts an older age and lower SFR. The right-hand panel of Figure 14 shows example SED fits for the galaxy Q0105-BX48. For this galaxy, SMC gave a significantly lower χ^2.

A.3. Comparison to Other SPS Models

For comparison with our fiducial model, we fit SEDs using the older BPASSv2.1 $Z_* = 0.002$ binary models with an upper mass cutoff of 100 $M_\odot$, including nebular continuum. We also fit SEDs using the BC03 $Z_* = 0.004$ and $Z_* = 0.020$ models (the latter of which is arguably the most commonly used SED model in the literature). We find that the χ^2 of the fits using both of these models were similar to those produced by our fiducial model. A detailed comparison between the four models used for SED fitting is beyond the scope of this work; however, the fractional changes in each fit parameter relative to their BPASSv2.2 100 $M_\odot$ binary model values are given in Table 4 (all assuming Calzetti et al. 2000 attenuation). Note that

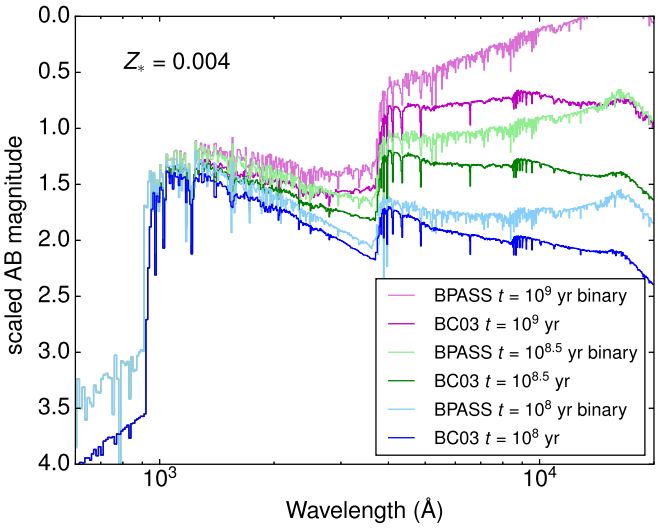

Figure 15. Comparison of BPASSv2.2 and BC03 model SEDs, where both models assume a metallicity of $Z_* = 0.004$. The SEDs are unreddened and unredshifted, and the BPASSv2.2 models shown here assume an upper mass cutoff of 100 $M_\odot$ with nebular continuum not included. The SEDs are compared at three different ages: $t = 10^8$ yr, $t = 10^{8.5}$ yr, and $t = 10^9$ yr. The BPASSv2.2 models are somewhat brighter than BC03 in the far-UV, the region most important for determining SFR_{SED}. This generally results in lower SFRs given by the BPASSv2.2 models.

Table 4
Parameters Relative to BPASSv2.2 $Z_* = 0.002$

Quantity	BPASSv2.1 $Z_* = 0.002$	BC03 $Z_* = 0.004$	BC03 $Z_\odot$
$E(B-V)_{SED}$	−0.02	0.00	−0.07
Age	0.00	+0.23	+0.65
M_*	−0.04	+0.17	+0.33
SFR_{SED}	−0.04	+0.10	−0.12

Note. All quoted values are the mean difference in dex between the parameters output by the given model and those output by the fiducial model used in this paper, BPASSv2.2 $Z_* = 0.002$ $M_{up} = 100$ $M_\odot$. Stellar masses and SFRs have been adjusted to account for the differences in IMF between the BPASS and BC03 models.

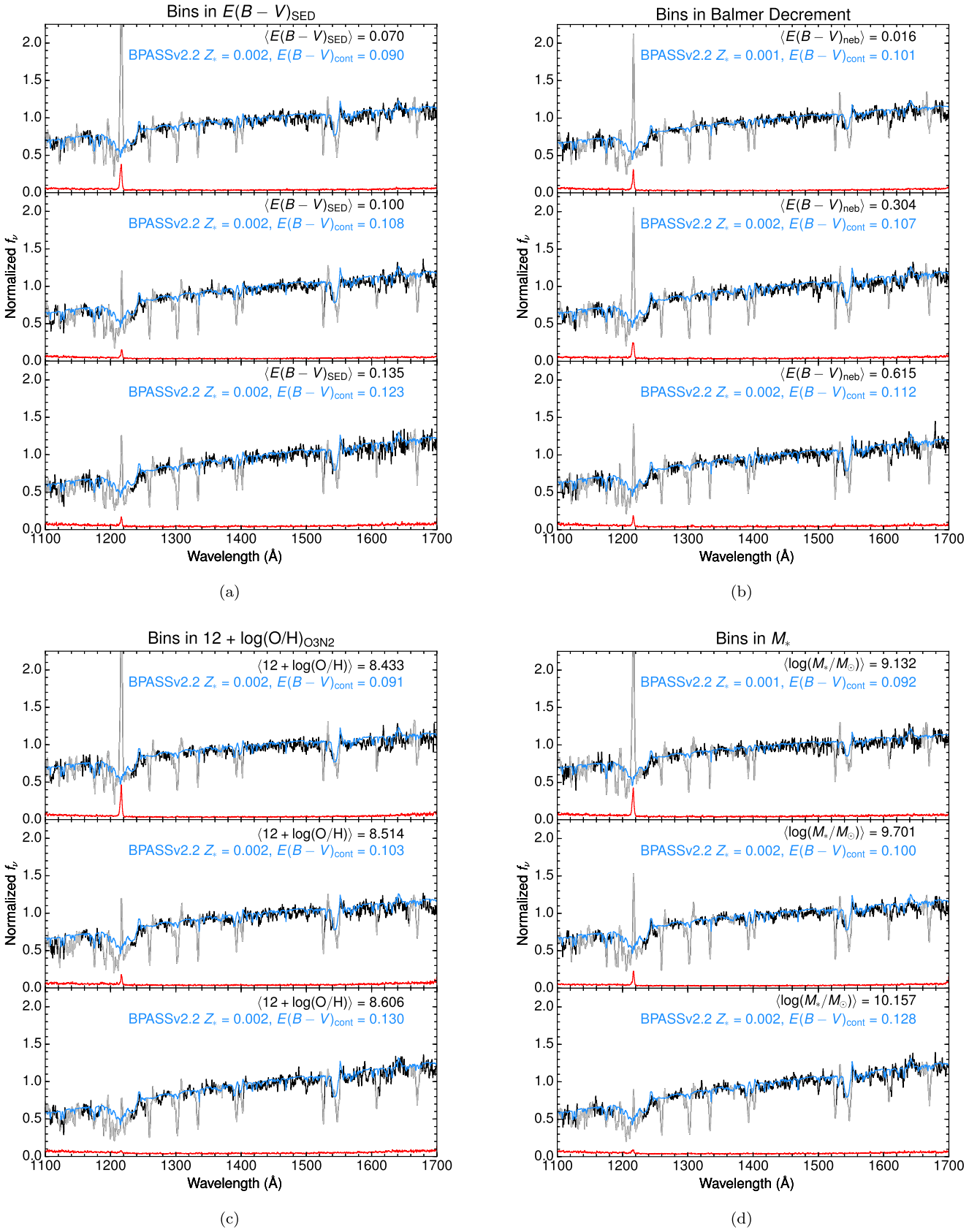

Figure 16. Stacked composite rest-frame UV spectra of the LRIS+MOSFIRE sample, in bins of (a) $E(B-V)_{\rm SED}$, (b) BD (converted to $E(B-V)_{\rm neb}$), (c) $12+\log({\rm O/H})_{\rm O3N2}$, (d) M_*, (e) ${\rm SFR}_{\rm H\alpha}$, and (f) ${\rm SFR}_{\rm SED}$. Bootstrapped error spectra are shown in red. Prior to stacking, the spectra were normalized by the median flux in the range 1400–1500 Å. Superposed are the best-fit population synthesis models from BPASSv2.2 (blue), reddened by the best-fit $E(B-V)_{\rm cont}$ (assuming an SMC attenuation curve), which was calculated by minimizing χ^2 with respect to the observed spectrum, after masking regions containing nebular emission lines or interstellar absorption lines (gray).

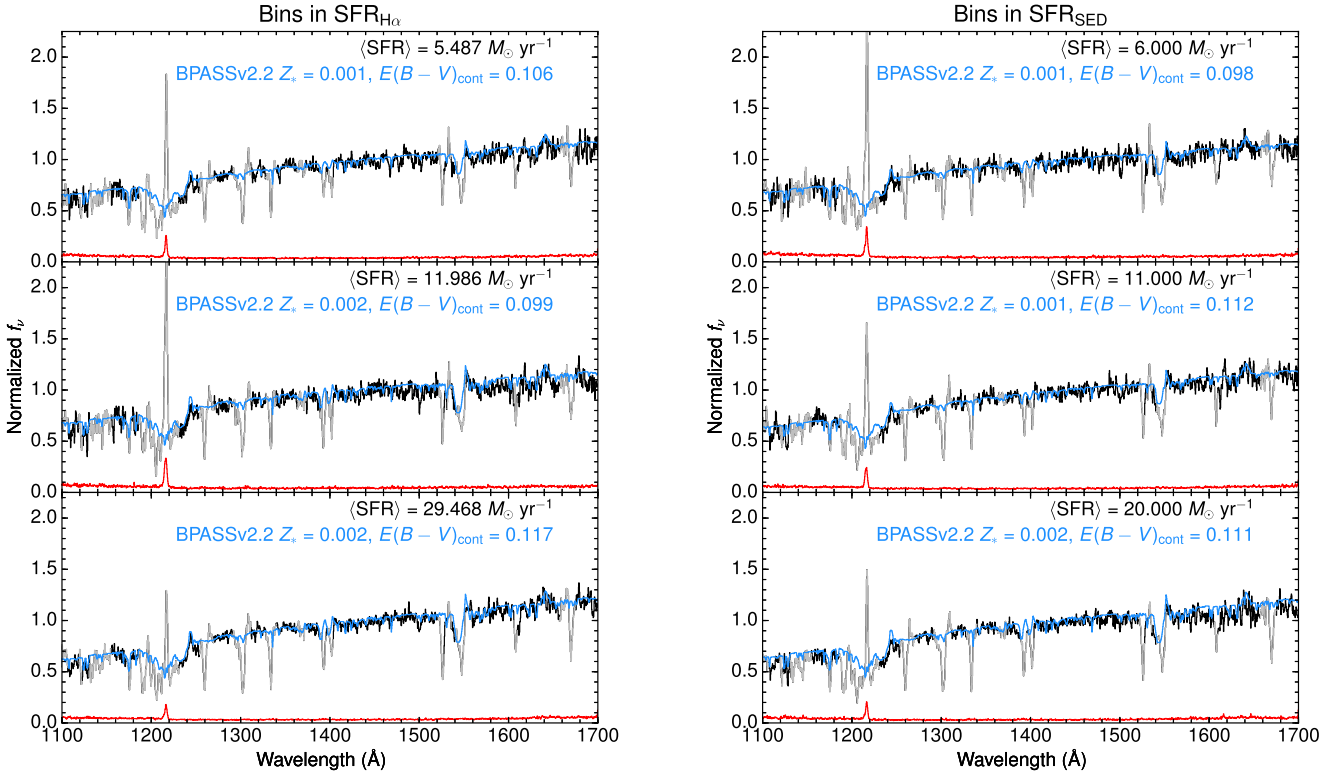

(e) (f)

Figure 16. (Continued.)

the BC03 models do not include the contribution from the nebular continuum.

We also fit SEDs using the BPASS models with an upper mass cutoff of 300 $M_\odot$ We found that changing the upper mass cutoff has almost no effect on any of the inferred parameters, due to the relative insensitivity of the integrated SED in the range 0.35–4.5 μm (or $\sim$1200 Å$-$1.5 μm in the rest frame) to the most massive stars; the primary difference between the two models is in the (unobservable) EUV spectrum, and thus, the predicted strengths of nebular emission lines and line ratios. We selected the 100 $M_\odot$ model as our fiducial model because the derivation of the Calzetti et al. (2000) curve assumes an upper mass IMF cutoff of 100 $M_\odot$. Table 4 compares the inferred SED fit parameters for the three models discussed in this paper.

Figure 15 compares the model SEDs for BPASSv2.2 and BC03 for three choices of stellar population age, where both models assume a metallicity of $Z_* = 0.004$, and nebular continuum is not included for the BPASSv2.2 models. The BPASSv2.2 models are somewhat brighter than BC03 blueward of the Balmer break at $t = 10^8$ yr, which is close to the median age predicted by the BC03 $Z_* = 0.020$ models.

Appendix B
Spectral Synthesis Fitting to Rest-UV Spectra

B.1. Generating the Composite Rest-UV Spectra

To generate the composite rest-UV spectra described in Section 4, the LRIS spectra were shifted to the rest frame using z_{neb}, and the sample was sorted into three equal-number bins of six quantities: $E(B-V)_{SED}$, $E(B-V)_{neb}$, $12 + \log(O/H)_{O3N2}$, M_*, $SFR_{H\alpha}$, and SFR_{SED}. The spectra were then spline-interpolated onto a rest wavelength scale of 0.35 Å/pixel, and two positive and negative extrema (four points total) were rejected at each dispersion pixel. The composite spectra were generated by normalizing each spectrum by the median flux density in the range 1400–1500 Å and averaging without weighting. The error spectra were generated by a bootstrap technique similar to that described by Trainor et al. (2015); over 1000 iterations, random spectra were drawn with replacement (the same number of spectra as in the bin) and stacked. Outlier rejection was performed on the bootstrap spectra in the same manner as the data. The standard deviation of the values at each pixel over all 1000 iterations was used to define the error spectrum associated with each stack. Thus, the error spectrum encompasses both the observational uncertainties in individual spectra and the intrinsic variation among galaxies in a given stack.

The composites were corrected for the mean opacity of the IGM due to neutral hydrogen along the line of sight using measurements from Rudie et al. (2013), for a source with $z = 2.40$ (this is close to the mean redshift of the sample; see Table 1). Details of this correction are described by Steidel et al. (2016), but we note that the IGM correction only affects the spectrum shortward of 1216 Å.

B.2. Spectral Synthesis Model Details

For fitting SPS models to the observed data, we used the far-UV spectra generated by the BPASSv2.2 model suite (Stanway & Eldridge 2018), assuming a constant SFH with an age of 10^8 yr (see Steidel et al. 2016 for details). We considered only models with an upper mass cutoff of 100 $M_\odot$ that include binary evolution, with stellar metallicities $Z_* = (0.001, 0.002, 0.003, 0.004, 0.006, 0.008, 0.010, 0.014)$. The stellar metallicity of the

model is allowed to vary independently of any knowledge of the gas-phase O/H in the three bins as a means of accounting for non-solar abundance ratios of O relative to Fe, where Z_* maps to Fe/H in the stars (Steidel et al. 2016; Strom et al. 2018). As with the SED fitting (Appendix A), we self-consistently included the nebular continuum contribution. The model spectra were normalized by the median flux in the range 1400–1500 Å in order to match the data.

For comparison with the observed spectra, the model spectra were spline-interpolated onto the pixel scale of each composite. We varied only the amount of stellar continuum reddening, which determines the "slope" of the spectrum. The model spectra were reddened with the Calzetti et al. (2000) and SMC attenuation curves, and the continuum color excess $E(B-V)_{\rm cont}$ was varied over the range $0.000 \leqslant E(B-V)_{\rm cont} \leqslant 0.600$ in steps of 0.001. Spectral regions corresponding to nebular emission lines and interstellar absorption lines were excluded from fitting; see Steidel et al. (2016) for details. The best-fit combination of Z_* and $E(B-V)_{\rm cont}$ for each spectral synthesis model was determined by computing the total χ^2, summed over all unmasked pixels. The minimum χ^2 was then compared for each attenuation curve, for each of the six binned quantities.

Figure 16 shows stacked composite rest-frame UV spectra of the LRIS+MOSFIRE sample, in bins of (a) $E(B-V)_{\rm SED}$, (b) BD (converted to $E(B-V)_{\rm neb}$), (c) $12+\log({\rm O/H})_{\rm O3N2}$, (d) M_*, (e) ${\rm SFR}_{\rm H\alpha}$, and (f) ${\rm SFR}_{\rm SED}$, overlaid with the best-fit spectral synthesis models from BPASSv2.2 (blue). For reasons of space, only the fits using the SMC curve are shown. The strong relationship between Lyα line strengths and various properties apparent in Figure 16 will be discussed in a future paper.

ORCID iDs

Rachel L. Theios https://orcid.org/0000-0002-4236-1037
Charles C. Steidel https://orcid.org/0000-0002-4834-7260
Allison L. Strom https://orcid.org/0000-0001-6369-1636
Gwen C. Rudie https://orcid.org/0000-0002-8459-5413
Ryan F. Trainor https://orcid.org/0000-0002-6967-7322
Naveen A. Reddy https://orcid.org/0000-0001-9687-4973

References

Abazajian, K. N., Adelman-McCarthy, J. K., Agüeros, M. A., et al. 2009, ApJS, 182, 543
Adelberger, K. L., & Steidel, C. C. 2000, ApJ, 544, 218
Adelberger, K. L., Steidel, C. C., Shapley, A. E., et al. 2004, ApJ, 607, 226
Álvarez-Márquez, J., Burgarella, D., Heinis, S., et al. 2016, A&A, 587, A122
Asplund, M., Grevesse, N., Sauval, A. J., & Scott, P. 2009, ARA&A, 47, 481
Bouwens, R. J., Aravena, M., Decarli, R., et al. 2016, ApJ, 833, 72
Bruzual, G., & Charlot, S. 2003, MNRAS, 344, 1000
Buat, V., Giovannoli, E., Heinis, S., et al. 2011, A&A, 533, A93
Calzetti, D., Armus, L., Bohlin, R. C., et al. 2000, ApJ, 533, 682
Calzetti, D., Kinney, A. L., & Storchi-Bergmann, T. 1994, ApJ, 429, 582
Capak, P. L., Carilli, C., Jones, G., et al. 2015, Natur, 522, 455
Cardelli, J. A., Clayton, G. C., & Mathis, J. S. 1989, ApJ, 345, 245
Charlot, S., & Fall, S. M. 2000, ApJ, 539, 718
Crowther, P. A. 2007, ARA&A, 45, 177
Daddi, E., Dannerbauer, H., Elbaz, D., et al. 2008, ApJL, 673, L21
Daddi, E., Dickinson, M., Morrison, G., et al. 2007, ApJ, 670, 156
Domínguez, A., Siana, B., Henry, A. L., et al. 2013, ApJ, 763, 145
Eldridge, J. J., Stanway, E. R., Xiao, L., et al. 2017, PASA, 34, e058
Erb, D. K., Steidel, C. C., Shapley, A. E., et al. 2006, ApJ, 647, 128
Esteban, C., García-Rojas, J., Carigi, L., et al. 2014, MNRAS, 443, 624
Gordon, K. D., Clayton, G. C., Misselt, K. A., Landolt, A. U., & Wolff, M. J. 2003, ApJ, 594, 279
Granato, G. L., Lacey, C. G., Silva, L., et al. 2000, ApJ, 542, 710
Heinis, S., Buat, V., Béthermin, M., et al. 2014, MNRAS, 437, 1268
Kashino, D., Silverman, J. D., Rodighiero, G., et al. 2013, ApJL, 777, L8
Kauffmann, G. 2014, MNRAS, 441, 2717
Kennicutt, R. C., & Evans, N. J. 2012, ARA&A, 50, 531
Kennicutt, R. C., Jr. 1998, ApJ, 498, 541
Koprowski, M. P., Coppin, K. E. K., Geach, J. E., et al. 2016, ApJL, 828, L21
Koprowski, M. P., Coppin, K. E. K., Geach, J. E., et al. 2018, MNRAS, 479, 4355
Kriek, M., & Conroy, C. 2013, ApJL, 775, L16
Kriek, M., Shapley, A. E., Reddy, N. A., et al. 2015, ApJS, 218, 15
Leitherer, C., Ekström, S., Meynet, G., et al. 2014, ApJS, 212, 14
Leitherer, C., & Heckman, T. M. 1995, ApJS, 96, 9
Madau, P., & Dickinson, M. 2014, ARA&A, 52, 415
Mannucci, F., Cresci, G., Maiolino, R., Marconi, A., & Gnerucci, A. 2010, MNRAS, 408, 2115
McLean, I. S., Steidel, C. C., Epps, H. W., et al. 2012, Proc. SPIE, 8446, 84460J
McLure, R. J., Dunlop, J. S., Cullen, F., et al. 2018, MNRAS, 476, 3991
Meurer, G. R., Heckman, T. M., & Calzetti, D. 1999, ApJ, 521, 64
Narayanan, D., Davé, R., Johnson, B. D., et al. 2018, MNRAS, 474, 1718
Nelson, E. J., van Dokkum, P. G., Momcheva, I. G., et al. 2016, ApJL, 817, L9
Nomoto, K., Tominaga, N., Umeda, H., Kobayashi, C., & Maeda, K. 2006, NuPhA, 777, 424
Oke, J. B., Cohen, J. G., Carr, M., et al. 1995, PASP, 107, 375
Osterbrock, D. E. 1989, Astrophysics of Gaseous Nebulae and Active Galactic Nuclei (Mill Valley, CA: Univ. Science Books)
Oteo, I., Bongiovanni, Á., Magdis, G., et al. 2014, MNRAS, 439, 1337
Pettini, M., & Pagel, B. E. J. 2004, MNRAS, 348, L59
Pilyugin, L. S., Grebel, E. K., & Mattsson, L. 2012, MNRAS, 424, 2316
Popping, G., Puglisi, A., & Norman, C. A. 2017, MNRAS, 472, 2315
Price, S. H., Kriek, M., Brammer, G. B., et al. 2014, ApJ, 788, 86
Reddy, N., Dickinson, M., Elbaz, D., et al. 2012a, ApJ, 744, 154
Reddy, N. A., Erb, D. K., Pettini, M., Steidel, C. C., & Shapley, A. E. 2010, ApJ, 712, 1070
Reddy, N. A., Kriek, M., Shapley, A. E., et al. 2015, ApJ, 806, 259
Reddy, N. A., Oesch, P. A., Bouwens, R. J., et al. 2018, ApJ, 853, 56
Reddy, N. A., Pettini, M., Steidel, C. C., et al. 2012b, ApJ, 754, 25
Reddy, N. A., & Steidel, C. C. 2004, ApJL, 603, L13
Reddy, N. A., Steidel, C. C., Fadda, D., et al. 2006, ApJ, 644, 792
Reddy, N. A., Steidel, C. C., Pettini, M., & Bogosavljević, M. 2016a, ApJ, 828, 107
Reddy, N. A., Steidel, C. C., Pettini, M., Bogosavljević, M., & Shapley, A. E. 2016b, ApJ, 828, 108
Rudie, G. C., Steidel, C. C., Shapley, A. E., & Pettini, M. 2013, ApJ, 769, 146
Rudie, G. C., Steidel, C. C., Trainor, R. F., et al. 2012, ApJ, 750, 67
Salim, S., Boquien, M., & Lee, J. C. 2018, ApJ, 859, 11
Sana, H., de Mink, S. E., de Koter, A., et al. 2012, Sci, 337, 444
Sanders, R. L., Shapley, A. E., Kriek, M., et al. 2016, ApJ, 816, 23
Seaton, M. J. 1979, MNRAS, 187, 73P
Shapley, A. E., Steidel, C. C., Erb, D. K., et al. 2005, ApJ, 626, 698
Shivaei, I., Kriek, M., Reddy, N. A., et al. 2016, ApJL, 820, L23
Shivaei, I., Reddy, N. A., Siana, B., et al. 2018, ApJ, 855, 42
Smit, R., Bouwens, R. J., Labbé, I., et al. 2016, ApJ, 833, 254
Sparre, M., Hayward, C. C., Feldmann, R., et al. 2017, MNRAS, 466, 88
Stanway, E. R., & Eldridge, J. J. 2018, MNRAS, 479, 75
Steidel, C. C., Erb, D. K., Shapley, A. E., et al. 2010, ApJ, 717, 289
Steidel, C. C., Rudie, G. C., Strom, A. L., et al. 2014, ApJ, 795, 165
Steidel, C. C., Shapley, A. E., Pettini, M., et al. 2004, ApJ, 604, 534
Steidel, C. C., Strom, A. L., Pettini, M., et al. 2016, ApJ, 826, 159
Strom, A. L., Steidel, C. C., Rudie, G. C., et al. 2017, ApJ, 836, 164
Strom, A. L., Steidel, C. C., Rudie, G. C., Trainor, R. F., & Pettini, M. 2018, ApJ, 868, 117
Tacconi, L. J., Genzel, R., Neri, R., et al. 2010, Natur, 463, 781
Trainor, R. F., Steidel, C. C., Strom, A. L., & Rudie, G. C. 2015, ApJ, 809, 89
Tremonti, C. A., Heckman, T. M., Kauffmann, G., et al. 2004, ApJ, 613, 898
Weisz, D. R., Johnson, B. D., Johnson, L. C., et al. 2012, ApJ, 744, 44
Zahid, H. J., Kewley, L. J., & Bresolin, F. 2011, ApJ, 730, 137